

# Correlated insulators and charge density wave states in chirally twisted triple bilayer graphene

Geng-Dong Zhou,<sup>1</sup> Yi-Jie Wang,<sup>1</sup> Wen-Xuan Wang,<sup>1</sup> Xiao-Bo Lu,<sup>1,2</sup> and Zhi-Da Song<sup>1,2,3,\*</sup>

<sup>1</sup>*International Center for Quantum Materials, School of Physics, Peking University, Beijing 100871, China*

<sup>2</sup>*Collaborative Innovation Center of Quantum Matter, Beijing 100871, China*

<sup>3</sup>*Hefei National Laboratory, Hefei 230088, China*

(Dated: May 22, 2024)

Motivated by recent experimental observations of displacement-field-tuned correlated insulators at integer and half-integer fillings in chirally twisted triple bilayer graphene (CTTBG), we study the single-particle and interacting physics of CTTBG. We find that there are two inequivalent stacking orders, *i.e.*, ABABBC and ABABAB, and both exhibit flat bands with nontrivial topology. We then use the Hartree-Fock approximation to calculate the rich phase diagram of CTTBG at all integer and half-integer fillings in both stacking orders and under the vertical displacement field. Under a small displacement field, the groundstates are flavor polarized states for ABABBC stacking order and intervalley coherent states for ABABAB stacking order at all integer and half-integer fillings. A larger displacement field will turn them into layer-polarized states. At half-integer fillings, the groundstates also exhibit charge density wave (CDW) order. For ABABAB stacking, the groundstates are always  $2 \times 1$  stripe state among a range of displacement fields. For ABABBC stacking, the groundstates are also  $2 \times 1$  stripe states under a small displacement field and a larger displacement will possibly favor further translation-symmetry-breaking, depending on filling and the direction of the displacement field. We demonstrate that the CDW states observed in the experiment can originate from the strong Coulomb interaction of the flat band electrons.

## I. INTRODUCTION

Moiré materials have drawn lots of attention as they provide highly tunable platforms to demonstrate the interplay of strong correlation effect and topology, which lead to exotic phenomena including correlated insulators [1–6], unconventional superconductivity [1–3, 6–8], Chern insulators [9–11], fractional Chern insulators [12–15], *etc.* A natural generalization of the first Moiré material magic-angle twisted bilayer graphene (TBG) is the family of twisted multilayer graphene [16, 17], including alternately and chirally twisted trilayer graphene [18–25], twisted double bilayer graphene [26–32], *etc.*, where superconductivity, correlated insulators, *etc.*, have also been observed. For multilayer Moiré material with more than one twisting interface, there will be multiple Moiré patterns and the stacking order of these Moiré patterns will play a significant role, which has been found in chirally twisted trilayer graphene [33, 34]. Among these multilayer graphene families, there is another interesting twisted multilayer Moiré material called chirally twisted triple bilayer graphene (CTTBG), which is formed by chirally stacked three Bernal bilayer graphenes with the same twist angle. It has been suggested to own robust flat bands [17] and studied in the recent experiments [35], where correlated gapped states at integer and half-integer fillings tuned by displacement field and magnetic field are found. Notably, Ref.[35] suggests that the correlated gapped states at non-integer fillings are charge density wave (CDW) states. A thorough study of the single-particle and interacting physics of CTTBG is needed to understand these insulating states observed in experiments.

In this work, we perform systematic single particle and Hartree-Fock study on CTTBG at all integer and half-integer

fillings at different displacement fields for two inequivalent stacking orders, which are denoted as ABABAB and ABABBC as detailed in Sec. II. At the single-particle level, we find that CTTBG in both stacking at  $\theta = 1.70^\circ$  possess a pair of flat bands separated from other bands, exhibiting non-trivial topology. In ABABBC-stacking CTTBG, we predict that one can also observe the valley hall effect when the Fermi level lies in the band gaps at fillings  $\pm 4$ . We also find that the flat band electrons in CTTBG are distributed dispersedly, in contrast to TBG where the flat band electrons are highly localized at the AA regions [36–39]. This underpins the significance of the nonlocal nature of Coulomb interactions and is consistent with the observed charge density wave states. Using the Hartree-Fock approximation, the groundstates at zero displacement field are found to be intervalley coherent (IVC) states in ABABAB stacking and flavor polarized states in ABABBC stacking. At a large displacement field, layer-polarized states are favored. At half-integer fillings, we find that groundstates further break the translation symmetry of the Moiré superlattice and this translation-symmetry-breaking can be tuned by the displacement field.

## II. MODEL AND METHOD

In this section, we discuss the stacking order of CTTBG and briefly summarize the model and notation we used.

### A. Geometry and stacking order

We consider CTTBG consisting of three Bernal-stacking bilayer graphenes twisted by angle  $(\theta, 0, -\theta)$  from top to bottom, and the experimental twist angle  $\theta$  is  $1.70^\circ$  [35]. The unrotated lattice vectors of the bilayer graphene are  $a_0(\pm\frac{1}{2}, \frac{\sqrt{3}}{2})$  where  $a_0 = 2.46\text{\AA}$  is the lattice constant. CT-

\* songzd@pku.edu.cn

TBG possesses two Moiré superlattices with lattice constant  $a_M = a_0/(2 \sin \frac{\theta}{2})$ , one formed by the top and middle layers and one by the middle and bottom layers. At the Moiré scale, the stacking order of CTTBG is decided by the displacement  $\mathbf{D}$  of the bottom Moiré pattern relative to the top Moiré pattern. These two Moiré patterns are also twisted by  $\theta$ , leading to a moiré-of-moiré structure with lattice constant  $\sim a_0/\theta^2 \approx 280\text{nm}$  when  $\theta = 1.70^\circ$  and the displacement  $\mathbf{D}$  will be position-dependent. However, similar to chirally and alternately twisted trilayer graphene [34, 40, 41], one expects that lattice relaxation will reconstruct the moiré-of-moiré lattice into domains which contain only single Moiré structure and they are separated by domain walls which form triangular or hexagonal networks. Within one domain,  $\mathbf{D}$  is uniform and takes a fixed value that is favored by lattice relaxation.

In this work, we consider a single domain with uniform displacement  $\mathbf{D} = (0, 0), \pm a_M(\frac{1}{\sqrt{3}}, 0)$  modulo the Moiré lattice vector, where CTTBG respects  $C_{3z}$  symmetry and the elastic energy reaches the local extremum. These three cases correspond to the ABAB-stacking region in the top Moiré pattern aligning with the ABAB/ABBC/ABCA-stacking region in the bottom Moiré pattern, respectively, and we denote them as ABABAB, ABABBC and ABABCA stacking orders. Besides,  $C_{2x}$  is preserved by each Bernal bilayer and swaps the top and bottom Moiré patterns, thus changing CTTBG with displacement  $\mathbf{D}$  to  $-C_{2x}\mathbf{D}$ . Therefore, the ABABAB stacking order further preserves  $C_{2x}$  symmetry, and the later two stacking orders can be transformed to each other under  $C_{2x}$ , for which we only need to consider two inequivalent stacking orders ABABAB and ABABBC, as shown in Fig. 1(a). There is no other spatial symmetry, hence the space groups are just  $D_3$  and  $C_{3z}$  for ABABAB-stacking and ABABBC-stacking CTTBG, respectively.

The favored displacement  $\mathbf{D}$  should be determined by minimizing the total energy. In Ref.[40], the authors pointed out that in twisted trilayer systems, whether a stacking order is favored can be inferred from whether the top and the bottom layer introduce the same or opposite tendency of deformation on the middle layer. As an example, we review the twisted trilayer graphene (TTG) cases in Ref.[40] here. We denote the local twist angles as  $(\theta_1, \theta_2, \theta_3)$  for the three layers, which are position-dependent as deformation is allowed. For each pair of adjacent layers, since AA regions cost more energy, the local twist angle tends to increase in AA regions and decrease in AB/BA regions, in order that AA regions shrink and AB/BA regions expand to save energy. Thus, for chiral TTG ( $\theta_1 > \theta_2 > \theta_3$ ), if AA region aligns AA region lattice relaxation tends to increase both  $\theta_1 - \theta_2$  and  $\theta_2 - \theta_3$ , which make  $\theta_2$  in dilemma. By contrast, if the AA region aligns with the AB region, one can simultaneously increase  $\theta_1 - \theta_2$  and decrease  $\theta_2 - \theta_3$ . As a result, AAB stacking is preferred over AAA stacking in chiral TTG. Conversely, in alternating TTG ( $\theta_1 > \theta_2, \theta_3 > \theta_2$ ) AAA stacking is preferred. These are confirmed by numerical calculation in [33, 40]. Based on the same principle, we do not perform lattice relaxation calculation but just argue that it also prefers ABABBC-stacking order in CTTBG. We list the stacking region and the tendency

of deformation in Table I, which shows that the deformations of two Moiré patterns are frustrated in all three stacking regions in ABABAB-stacking CTTBG and in only one stacking region in ABABBC-stacking CTTBG, akin to chiral TTG. However, this is not a quantitative calculation, and the corrugation, the energy of the electron, and the electron-phonon coupling are not fully considered, so the ABABAB-stacking order is not ruled out. Thus, we performed calculations on both stacking orders in this work.

	ABABAB			Favorable	ABABBC			Favorable
twist angle	$\theta$	$\delta\theta$	$-\theta$	$\searrow$	$\theta$	$\delta\theta$	$-\theta$	$\searrow$
relative twist angle	$\theta - \delta\theta$		$\theta + \delta\theta$	$\searrow$	$\theta - \delta\theta$		$\theta + \delta\theta$	$\searrow$
Region	AA( $\uparrow$ )	AA( $\uparrow$ )	$\times$		AA( $\uparrow$ )	AB( $\downarrow$ )	$\checkmark$	
	BA( $\downarrow$ )	BA( $\downarrow$ )	$\times$		BA( $\downarrow$ )	AA( $\uparrow$ )	$\checkmark$	
	AB( $\downarrow$ )	AB( $\downarrow$ )	$\times$		AB( $\downarrow$ )	BA( $\downarrow$ )	$\times$	

TABLE I. The local deformation of each layer. The second row shows the twist angle of each bilayer, and the third row shows the twist angle of the top layer relative to the bottom layer in each Moiré pattern. The 4-6th rows show the stacking regions and the tendency of deformation of the local relative twist angles. The stacking regions are labeled only by the atoms in adjacent monolayers instead of bilayers, *e.g.*, by BA-stacking instead of ABAB-stacking.  $\uparrow$  ( $\downarrow$ ) means that the local relative twist angle tends to increase (decrease).

## B. Non-interacting model

Here we briefly summarize the non-interacting model and more details can be found in Appendix A. With the  $i$ -th bilayer (counted from top to bottom) displaced by  $\mathbf{d}_i$ , the non-interacting continuum model [16, 42, 43] of CTTBG reads

$$\hat{H}_0 = \hat{H}_{BM} + \hat{H}_V, \quad (1)$$

$$\hat{H}_{BM} = \int d^2\mathbf{r} \left[ \sum_{i=1}^3 \sum_{\eta s, aa'} c_{i\mathbf{r}a\eta s}^\dagger h_{aa'}^\eta (-i\nabla_{\mathbf{r}}) c_{i\mathbf{r}a'\eta s} + \left( \sum_{i=1}^2 \sum_{\eta, s} \sum_{aa'} [T_\eta^{i,i+1}(\mathbf{r})]_{aa'} c_{i\mathbf{r}a\eta s}^\dagger c_{i\mathbf{r}a'\eta s} + h.c. \right) \right], \quad (2)$$

where

$$h^\eta(\mathbf{k}) = \frac{\sqrt{3}}{2} \gamma_0 a_0 \sigma_0 \otimes (\eta k_x \sigma_x + k_y \sigma_y) + \begin{pmatrix} 0 & 0 & 0 & \gamma_1 \\ 0 & 0 & 0 & 0 \\ 0 & 0 & 0 & 0 \\ \gamma_1 & 0 & 0 & 0 \end{pmatrix} \quad (3)$$

is the low energy Hamiltonian of Bernal-stacking bilayer graphene near the Dirac cone at  $\eta\mathbf{K} = \eta(\frac{4\pi}{3a_0}, 0)$ ,  $\eta = \pm$ ,  $\sigma_{0,x,y}$  are the Pauli matrices and

$$[T_\eta^{i,i+1}(\mathbf{r})]_{aa'} = \sum_n \left[ \begin{pmatrix} 0 & 0 \\ 1 & 0 \end{pmatrix} \otimes T_n \right]_{aa'} e^{i\eta\mathbf{q}_n \cdot [\mathbf{r} - \mathbf{D}_{i,i+1}]} \quad (4)$$

describes the Moiré hopping. We adopt the hopping parameters  $\gamma_0 = 2610\text{meV}$ ,  $\gamma_1 = 361\text{meV}$ , which are defined in Fig. 1(a).  $T_n = w_0\sigma_0 + w_1\sigma_x \cos \frac{2(n-1)\pi}{3} + w_1\sigma_y \sin \frac{2(n-1)\pi}{3}$  where  $w_0 = 88\text{meV}$ ,  $w_1 = 110\text{meV}$  are AA and AB/BA hopping, respectively. The sublattice index  $a(a')$  labels the atoms in a unit cell with order (1A,1B,2A,2B).  $c_{i\mathbf{r}a\eta s}$  annihilates an electron in the  $i$ -th bilayer at position  $\mathbf{r}$  in  $\eta$  valley with spin  $s$  and sublattice index  $a$ .  $\mathbf{q}_n = C_{3z}^{n-1}k_\theta(0, -1)$ , where  $k_\theta = 2|\mathbf{K}|\sin \frac{\theta}{2}$ .  $\mathbf{D}_{i,i+1} = \frac{\hat{z}}{2\sin(\theta/2)} \times (\delta_1 + \mathbf{d}_i - \mathbf{d}_{i+1})$  is the location of the AA region in the Moiré pattern formed by the  $i$ -th and  $(i+1)$ -th bilayer,  $\delta_1 = -\frac{a_0}{\sqrt{3}}(0, 1)$  is the position of A sublattice relative to the B sublattice in the same unit cell and the same layer, and the displacement of two Moiré patterns is  $\mathbf{D} = \mathbf{D}_{23} - \mathbf{D}_{12}$ . We also neglect other terms like long-range hopping and leave the discussion of their influence to Appendix A.

Additionally, we add a layer-dependent on-site potential  $\hat{H}_V$  which brings  $V_d(l - \frac{7}{2})$  for the  $l$ -th monolayer graphene, which reflects both the gate-induced displacement field and internal displacement field from charge redistribution among layer. In principle, the potential brought by the latter one is not linear with  $l$  [44, 45] but we neglect this effect for simplicity [46]. The space groups of both stacking orders are  $C_{3z}$  with displacement field since it does not respect  $C_{2x}$  symmetry.

We also summarize the symmetry of the model, as shown in Table II. Despite the space group symmetry mentioned above, the model also respects  $U(2) \times U(2)$  symmetry, consisting of charge  $U(1)_c$ , valley  $U(1)_v$ , and spin  $SU(2)_\pm$  in  $\eta = \pm$  valley, as we have neglected spin-orbital couplings and Umklapp scattering term as done in previous work [47–53].

Furthermore, when  $\mathbf{D}_{i,i+1}$  lies in  $x$  direction, i.e.,  $\mathbf{d}_i - \mathbf{d}_{i+1}$  lies in  $y$  direction, which is satisfied for both ABABAB and ABABBC stacking orders, Eq. (2) also has an approximate particle-hole (PH) symmetry  $\mathcal{P}_y$  which anticommutes with the single particle Hamiltonian  $H_{BM}$ . Similar to the PH symmetry in TBG [54],  $\mathcal{P}_y$  will be broken when quadratic terms of  $\mathbf{k}$  or  $\theta$ -dependence are included in  $h^\eta(\mathbf{k})$ .  $\mathcal{P}_y$  is antiunitary and its matrix representation is  $D_{ia\eta, i'a'\eta'}(\mathcal{P}_y) = (-1)^{l_{ia}}\delta_{aa'}\delta_{\eta\eta'}$  where  $l_{ia} = 1, \dots, 6$  labels the monolayer, to which the  $a$  sublattice in the  $i$ -th bilayer belongs, from top to bottom.  $\mathcal{P}_y$  also changes  $\mathbf{r}$  to  $M_y\mathbf{r}$ , and hence  $\mathbf{k}$  to  $C_{2y}\mathbf{k}$ . One can directly verify the anticommuting relation between  $\mathcal{P}_y$  and the intra-bilayer single-particle Hamiltonian, and also the Moiré coupling terms by making use of  $(T_1)^* = T_1, (T_2)^* = T_3, M_y\mathbf{q}_1 = -\mathbf{q}_1, M_y\mathbf{q}_2 = -\mathbf{q}_3$  and  $\mathbf{q}_1 \cdot \mathbf{D}_{i,i+1} = 0, \mathbf{q}_2 \cdot \mathbf{D}_{i,i+1} = -\mathbf{q}_3 \cdot \mathbf{D}_{i,i+1}$  given  $\mathbf{D}_{i,i+1}$  lies in  $x$  direction. Besides,  $\mathcal{P}_y$  commutes with the single particle Hamiltonian  $H_V$ , so at finite displacement field, the model is not invariant under  $\mathcal{P}_y$  but is related to the case with the displacement field reversed, i.e., CTTBG at filling  $\nu$  under displacement field  $V_d$  is equivalent to CTTBG at filling  $-\nu$  under displacement field  $-V_d$ .

The model also respects the spinless time-reversal symmetry (TRS)  $T_0 = \tau_x K$ , which  $T_0^2 = 1$ . Combined with  $U(1)_V$  we can define another TRS-like symmetry  $T_K = e^{-i\pi\tau_z/2}T_0 = \tau_y K$  where  $T_K^2 = -1$ .

Stacking	$V_d$	Space Group	$\mathcal{P}_y$	On-site
ABABAB	0	$D_3$	$\checkmark$	$U(2) \times U(2)$ , TRS
	$\neq 0$	$C_{3z}$	$\times$	
ABABBC	0	$C_{3z}$	$\checkmark$	
	$\neq 0$	$C_{3z}$	$\times$	

TABLE II. Symmetry of the model

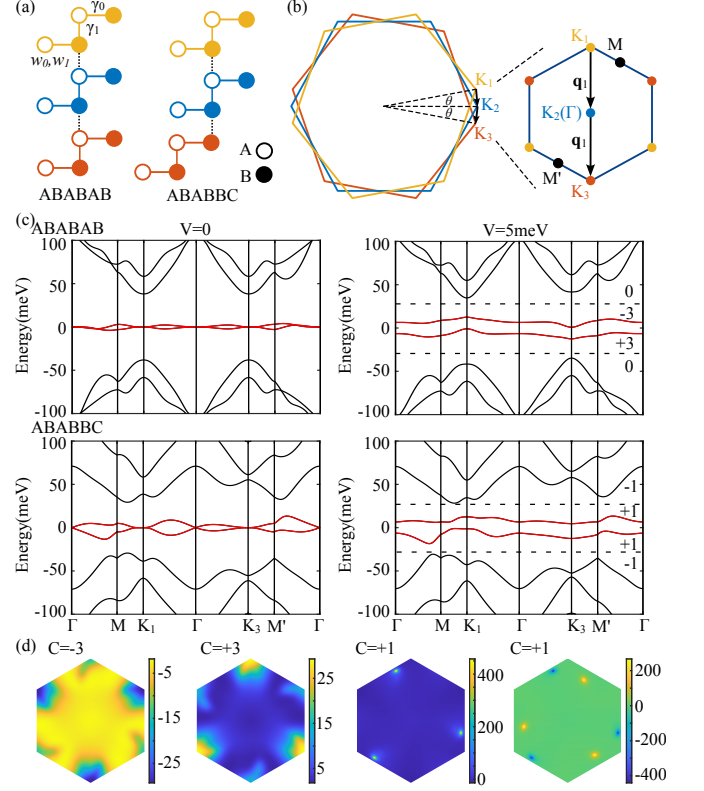


FIG. 1. (a) Geometry of the two stacking orders, viewed from  $x$  direction. The couplings are also indicated here. (b) Left: The graphene Brillouin zone. Right: the MBZ. (c) The non-interacting bands in  $\eta = +$  valley. The stacking orders in the upper and lower panels are ABABAB and ABABBC, respectively, and the displacement fields applied are  $V = 0$  and  $V = 5\text{meV}$  for the left and right panels. The numbers mark the total Chern number of the remote conduction bands, the flat conduction band, the flat valence band, and the remote valence bands from top to bottom, respectively. (d) From left to right: the Berry curvature of conductance, valence flat band in ABABAB stacking and conductance, valence flat band in ABABBC stacking under  $V_d = 5\text{meV}$ . The Berry curvature is normalized in the convention that the area of MBZ is  $4\pi^2$ .

### C. Interacting model and Hartree-Fock method

In this subsection, we discuss the interacting model and the Hartree-Fock (HF) method. The total Hamiltonian is  $\hat{H} = \hat{H}_0 + \hat{H}_I$  where  $\hat{H}_I = \frac{1}{2\Omega_{tot}} \sum_{\mathbf{q} \in \text{MBZ}} \sum_{\mathbf{G}} V(\mathbf{q} + \mathbf{G}) \delta \rho_{\mathbf{q}+\mathbf{G}} \delta \rho_{-\mathbf{q}-\mathbf{G}}$  where  $\delta \rho_{\mathbf{q}+\mathbf{G}}, V(\mathbf{q} + \mathbf{G})$  is the  $\mathbf{q} + \mathbf{G}$  component in the momentum space of the density operator relative to the charge background and the electron-electron interaction,  $\Omega_{tot}$  is the total area of the sample and MBZ

is the Moiré Brillouin zone, as shown in Fig. 1(b). We adopt the double-gate-screened Coulomb interaction  $V(\mathbf{q}) = \frac{e^2}{2\epsilon|\mathbf{q}|} \tanh \frac{\xi|\mathbf{q}|}{2}$ , where  $\xi = 30\text{nm}$  is the distance between the top and the bottom gates,  $\epsilon \sim 6$  is the dielectric constant of hBN.

To determine the groundstates at various fillings, we perform a projected HF calculation on the flat bands similar to previous works [47–53], whose details can be found in Appendix B. Diagonalizing  $\hat{H}_0$  we obtain a set of eigenenergy  $\epsilon_{\mathbf{k}m\eta}$  and eigenstate  $c_{\mathbf{k}m\eta s}$  where  $m$  is the band index. The total Hamiltonian in this basis is

$$\hat{H} = \sum_{\mathbf{k}n\eta s} \epsilon_{\mathbf{k}n\eta} c_{\mathbf{k}n\eta s}^\dagger c_{\mathbf{k}n\eta s} + \frac{1}{2\Omega_M} \sum_{\mathbf{k}\mathbf{k}'\mathbf{q}} \sum_{\substack{m\eta s \\ m'\eta' s'}} c_{\mathbf{k}m\eta s}^\dagger c_{\mathbf{k}+\mathbf{q}m\eta s} c_{\mathbf{k}'m'\eta' s'} c_{\mathbf{k}'-\mathbf{q}m'\eta' s'}^\dagger \quad (5)$$

where  $c_{\mathbf{k}m\eta s}^\dagger c_{\mathbf{k}'m'\eta' s'}^\dagger$  is defined as  $c_{\mathbf{k}m\eta s}^\dagger c_{\mathbf{k}'m'\eta' s'}^\dagger - \frac{1}{2}\delta_{\mathbf{k}\mathbf{k}'}\delta_{mm'}\delta_{\eta\eta'}\delta_{ss'}$  to avoid double counting. Since the parameters we used are from DFT calculation which already contains the self-consistent Hartree potential, we use the high-temperature subtraction scheme where the interaction in the density is measured with respect to the reference density with all bands half-filling at infinite temperature. In this scheme projecting Eq. (5) to the flat bands can be simply achieved by restricting  $m$  to the flat bands, as detailed in Appendix B, and we label them as  $m = 1, 2$  hereafter.

To discuss possible translation-symmetry-breaking order, we enlarge the unit cell, which yields a folded Moiré Brillouin zone (fMBZ). Each type of translation-symmetry-breaking order is labeled by the fMBZ and its reciprocal lattice vectors  $\mathbf{Q}_1, \mathbf{Q}_2$ , where electrons can be scattered into states with momenta differed by an integer multiple of  $\mathbf{Q}_{1,2}$ . We rewrite the momentum in MBZ as  $\mathbf{k} + \mathbf{Q}_b$  where  $\mathbf{k}$  lies in fMBZ and  $\mathbf{Q}_b$  lies in MBZ and is an integer multiple of  $\mathbf{Q}_{1,2}$ . We list the fMBZs we consider in Fig. 5(a). We then perform standard HF decomposition for Eq. (5), where the order parameters are  $O_{bm\eta s, b'm'\eta' s'} = \langle c_{\mathbf{k}+\mathbf{Q}_b m\eta s}^\dagger c_{\mathbf{k}+\mathbf{Q}_b' m'\eta' s'} \rangle - \frac{1}{2}\delta_{bb'}\delta_{mm'}\delta_{\eta\eta'}\delta_{ss'}$ . We start from random order parameters ( $\sim 100$  samples) and self-consistently calculate order parameters and total energies until they converge. Furthermore, we use the optimal damping method introduced by [55] to accelerate the convergence.

Here, we introduce several quantities to describe the symmetry of the mean-field solution. We first choose the gauge such that the spin up and the spin down wavefunction are the same and the wavefunction in  $\eta = -$  valley are related to the wavefunction in  $\eta = +$  valley by TRS, as detailed in Appendix B. There is a remaining gauge degree of freedom that one can choose the basis to be any linear combination of the two flat bands. We work either in the non-interacting energy band basis or the Chern basis introduced later, and the symmetry-breaking quantities we defined here do not depend on this gauge choice. Unless otherwise specified, we use  $\sigma_\mu, \tau_\mu, \varsigma_\mu, \mu = 0, x, y, z$  to refer to Pauli matrices acting on band index, valley, and spin degree of freedom. For con-

tinuous symmetry operation  $e^{-i\theta\hat{\Theta}}$  with generator

$$\hat{\Theta} = \frac{1}{2} \sum_{\mathbf{k} \in \text{fMBZ}} \sum_b \sum_{\substack{m\eta s \\ m'\eta' s'}} \Theta_{m'\eta' s', m\eta s} c_{\mathbf{k}+\mathbf{Q}_b m\eta s}^\dagger c_{\mathbf{k}+\mathbf{Q}_b m'\eta' s'} \quad (6)$$

where  $\Theta$  will be defined for each symmetry later, the symmetry-breaking strength can be defined by the norm of the commutator of the order parameter and the generator

$$\mathcal{S}_\Theta = \frac{1}{N_M} \sum_b \sum_{\mathbf{k}} (||[O_{bb}(\mathbf{k}), \Theta]||)^2 \quad (7)$$

where  $||\cdot||$  is defined by  $||A|| \equiv \sqrt{\text{Tr}(A^\dagger A)}$  for any matrix  $A$ , and  $O_{b''b'}(\mathbf{k})$  in Eq. (7) is an eight-by-eight matrix defined by  $(O_{b''b'}(\mathbf{k}))_{m\eta s, m'\eta' s'} = O_{b''m\eta s, b'm'\eta' s'}(\mathbf{k})$  (only  $b' = b'' = b$  used here). For valley U(1)  $\Theta = \sigma_0 \tau_z \varsigma_0$  and we denote the breaking strength as  $\mathcal{S}_V$ ; We define  $\mathcal{S}_{s\pm} = \frac{1}{4} \sum_{i=x,y,z} \mathcal{S}_{\sigma_0 \tau_\pm \varsigma_i}$  for SU(2) within  $\pm$  valley, where  $\sigma_i, \tau_i, \varsigma_i$  are the Pauli matrices act on the spin/valley degree of freedom, and  $\tau_\pm = \frac{\tau_0 \pm \tau_z}{2}$ . For example, if the order parameter takes the form  $\frac{1}{2}\tau_x \sigma_0 \varsigma_0$  at each  $\mathbf{k}$ , which means that  $\nu = 0$  and there are 4 electrons per unit cell among flat bands occupying the equal superposition of two valleys, one will have  $\mathcal{S}_V = 8$ ,  $\mathcal{S}_{s\pm} = 0$ ; if the order parameter is  $\frac{\sigma_0 + \sigma_z}{2} \frac{\tau_0 + \tau_z}{2} \frac{\varsigma_0 + \varsigma_z}{2} - \frac{1}{2}\sigma_0 \tau_0 \varsigma_0$ , which means there is one spin-up electron occupying  $\eta = +$  valley,  $\mathcal{S}_V = \mathcal{S}_{s-} = 0$  and  $\mathcal{S}_{s+} = 1$ . Furthermore  $\mathcal{S}_V, \mathcal{S}_{s\pm}$  are invariant under all of charge/valley U(1) and spin SU(2) $_{\pm}$  transformation and independent of the gauge choice among two flat bands, which are proved in Appendix B 4.

### III. RESULTS

#### A. Single particle band, topology and valley Hall effect

We plot the non-interacting bands in  $\eta = +$  valley for the two stacking orders with and without vertical field in Fig. 1(c). We find that all of them have two flat bands near the Fermi level separated from other bands, and in ABABAB-stacking CCTBG, the bands are flatter. The bandwidth is around 2meV for the ABABAB-stacking order and around 10meV for the ABABBC-stacking order. The total Chern numbers of the two flat bands in  $\eta = +$  valley are 0 and 2 for ABABAB and ABABBC-stacking CCTBG, respectively. The total Chern numbers for the remote valence bands in  $\eta = +$  valley are 0 and  $-1$  for ABABAB and ABABBC-stacking CCTBG, respectively. Thus, for ABABBC-stacking CCTBG at fillings  $\nu = \pm 4$ , the valley Chern number for filled bands is  $\pm 1$ , implying the valley Hall effect. We also plot the real space density distribution of the filled flat bands in Fig. 2. We find that the density is uniform in the top and bottom layers, and is more concentrated in the AA stacking region of the Moiré pattern formed by the twisted adjacent layers in the middle layers. The AA stacking region of the top Moiré pattern is



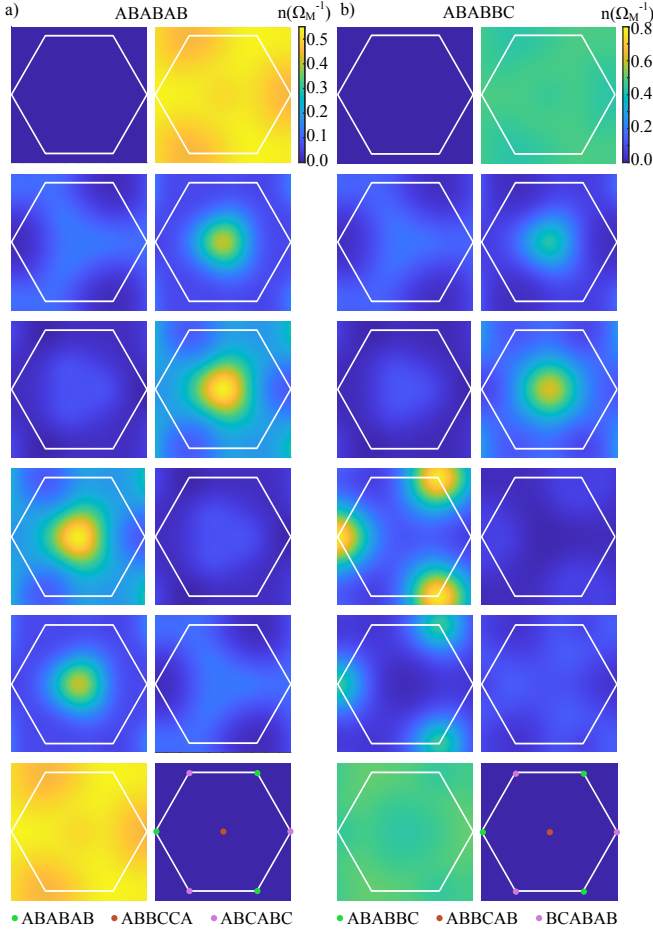


FIG. 2. The density profile of filled flat bands for (a) ABABAB stacking and (b) ABABBC stacking order. The density distribution on the A/B sublattice and each monolayer graphene from top to bottom also lie from left to right and from top to bottom, respectively. The regions of different stacking orders are marked in the last figure of each subfigure. Notice that the color codes are the same for the same stacking order and different for different stacking orders, and the origin point adapted in the model in Secs. IIB and IIC is located in the ABABAB or ABABBC region.

aligned with the AA stacking region of the bottom Moiré pattern in ABABAB-stacking CTTBG, and the AB stacking region in ABABBC-stacking CTTBG, and so are the localized centers of charge density distribution, as shown by Fig. 2.

Applying a vertical electric field, the two flat bands are separated, and each of them may have nontrivial topological properties. The Chern numbers of valence/conductance flat band are  $+3/-3$  and  $+1/+1$  in these two stackings, respectively, if we apply an electric field in  $z$  direction, as shown in Fig. 1(c) and  $-3/+3$  and  $+1/+1$  with the electric field at  $-z$  direction. The  $\pm 3$  Chern band in ABABAB-stacking CTTBG has already been reported in Ref.[17]. We also plot the berry curvature of each band in Fig. 1(d)(e), where one can see that the berry curvature is more uniform in ABABAB-stacking and more concentrated in ABABBC-stacking, which means that if both stackings are experimentally achievable the

previous may act as a better candidate to realize fractional Chern insulator [56, 57]. Here we emphasize that as the gap between the two flat bands is small, effects like next nearest neighbor hoppings may close this gap and let the Chern number for each band be ill-defined, which is shown in Fig. 7(b) in Appendix A. In either stacking, the gaps between the flat bands and the remote bands are larger; the valley Hall effects in ABABBC stacking at  $\nu = \pm 4$  are more robust, as one can see in Fig. 7(b) that after adding other terms, the total Chern number of the flat bands and the remote conduction/valence bands are invariant separately.

We also diagonalize the sublattice operators in the flat band subspace in the absence of displacement field and label them by  $(\tau, \sigma, s)$ , where  $\sigma = A(B)$  corresponds to the bands with more components from A(B) sublattice, yielding a Chern band basis similar to those used in [34, 47, 58–60]. The Chern number of these bands are:  $C_{\pm, A, s} = \mp 3, C_{\pm, B, s} = \pm 3$  for ABABAB stacking order and  $C_{\pm, A, s} = \mp 2, C_{\pm, B, s} = \pm 4$  for ABABBC stacking order.

### B. Correlated insulator states at integer fillings

In this section we discuss the translational symmetric solutions at all integer fillings. As we will show in the next subsection, with the parameters we adopt, they are indeed the groundstates. With the aid of  $\mathcal{P}_y$ , which flips  $\nu$  and  $V_d$ , we can only study  $\nu \geq 0$  cases, and for ABABAB-stacking order, further with  $C_{2x}$  symmetry which flips  $V_d$ , we can only study  $\nu \geq 0, V_d \geq 0$  cases.

We first study ABABBC-stacking CTTBG in the absence of a displacement field. We find that in the absence of a vertical electric field, the groundstates at integer fillings are gapped and valley and/or spin-polarized states. Besides, among each valley the spin polarization at each  $k$  points towards the same direction. We can classify the groundstates by their fillings of each valley and spin sector per Moiré unit cell, as shown in Table III. We have applied  $SU(2)_+ \times SU(2)_-$  rotation to choose the spin polarization in  $z$  direction. As an example, the degenerate groundstates at  $\nu = 0$  include

- spin-polarized or spin-valley-locked states. These states break  $SU(2)_+ \times SU(2)_-$  symmetry but preserve a time reversal symmetry. As an example, one of these states has four spin-up electrons, and two lie in  $\eta = +$  valley and two in  $\eta = -$  valley. This state respects the spinless time reversal symmetry  $T_0$ . Other states are the  $SU(2)_+ \times SU(2)_-$  partners of this state and respect a certain combination of  $T_0$  and  $SU(2)_+ \times SU(2)_-$  rotation.
- valley polarized state with four electrons polarized in one valley. This state preserves  $SU(2)_+ \times SU(2)_-$  but breaks TRS.

The two sets of states above are degenerate but are not related by symmetry. Instead, as detailed in Appendix B5, some operations like acting  $T_0$  to one spin sector of the order parameters can change one state to the other without changing HF

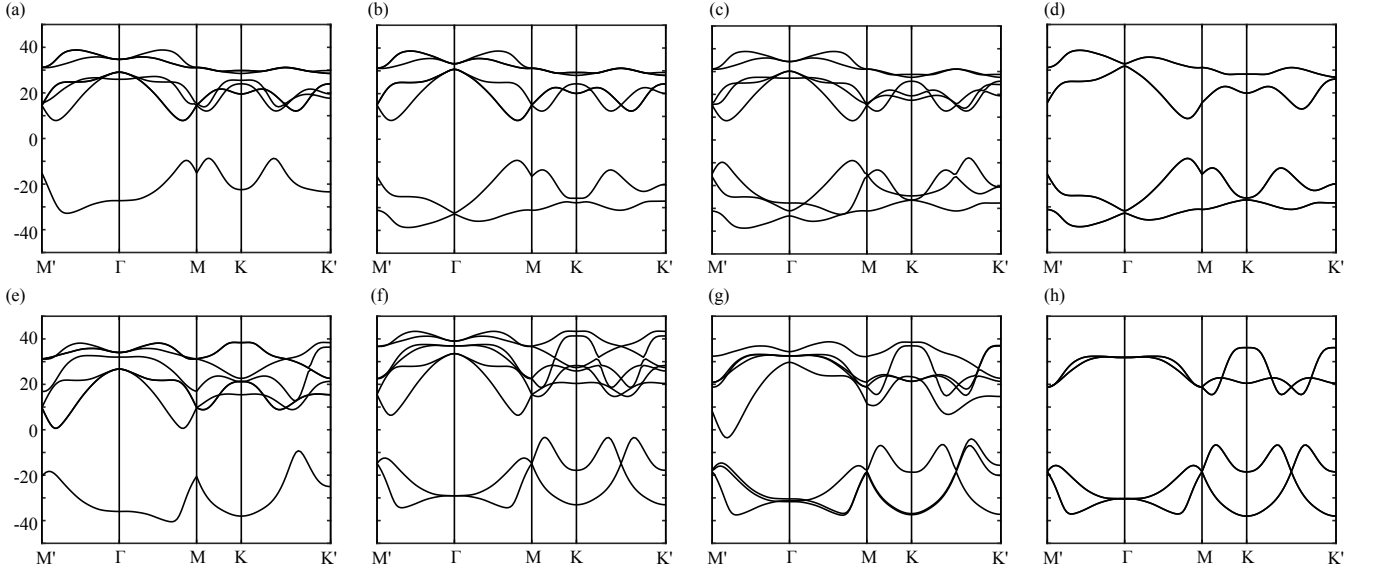


FIG. 3. The HF bands for ABABBC stacking order at integer fillings. From (a-d):  $V_d = 0 \text{ meV}$ ,  $\nu = -3, -2, -1, 0$ . From (e-h)  $V_d = 5 \text{ meV}$ ,  $\nu = -3, -2, -1, 0$ . Here, we only show one type of groundstate, even for those fillings with different types of groundstates. The calculations are performed on  $8 \times 8$  momentum lattice.

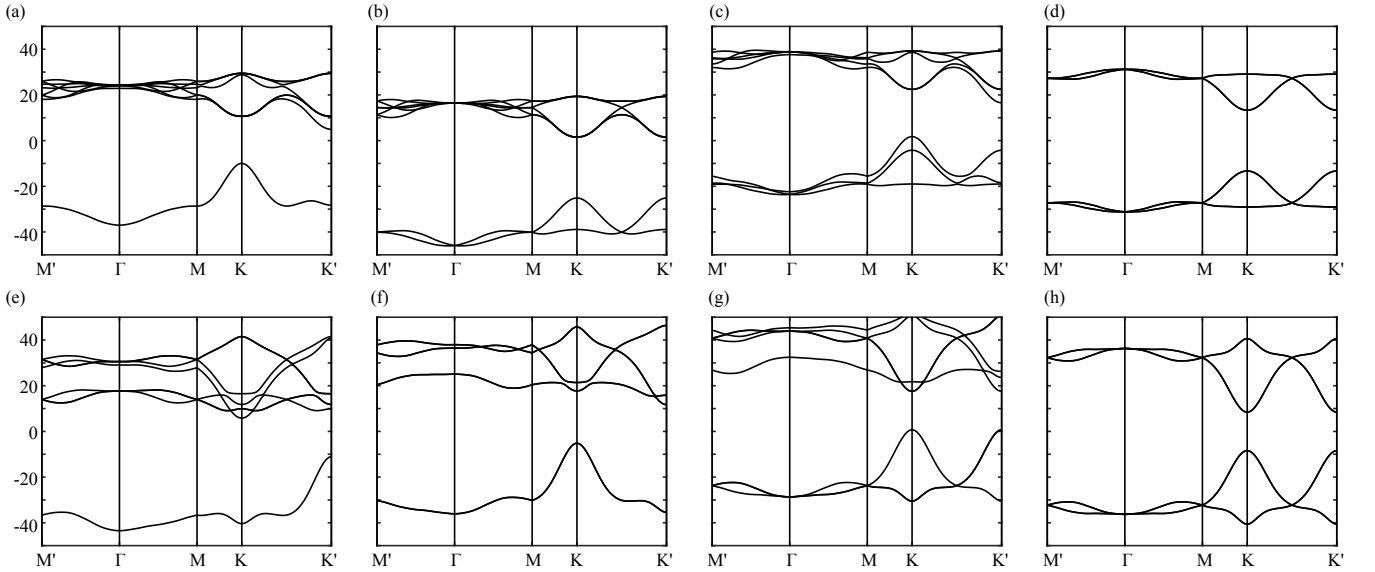


FIG. 4. The HF bands for ABABAB stacking order at integer fillings. From (a-d):  $V_d = 0 \text{ meV}$ ,  $\nu = -3, -2, -1, 0$ . From (e-h)  $V_d = 5 \text{ meV}$ ,  $\nu = -3, -2, -1, 0$ . Here, we only show one type of groundstate, even for those fillings with different types of groundstates. The calculations are performed on  $8 \times 8$  momentum lattice.

energy functional. This degeneracy is the consequence of the HF approximation and should be lifted by fluctuations upon the HF saddle points. Previous studies [34, 48] have also reported this degeneracy, and it is called "flavor permute symmetry" in Ref.[34]. For groundstates at  $\nu = \pm 2$ , we find that two electrons/holes tend to occupy different bands and maximize their total spin/valley polarization, which is similar to Hund's rule.

The groundstates of ABABAB-stacking CTTBG at  $V_d = 0$

are completely different from that of ABABBC-stacking CTB TG, where the groundstates are IVC states at all integer fillings, which break  $U(1)_V$  maximally as we find  $\mathcal{S}_V$  around  $2\nu$  at filling  $\nu$ . At fillings  $\nu = 0, \pm 2$  we find that the groundstates also preserve the Kramers TRS but do not preserve spinless TRS. In terms of the Chern basis introduced at the end of Sec. III A, we find that IVC happens mainly in the bands with the same Chern number in ABABAB-stacking CTTBG, which is similar to IVC groundstates in TBG. In ABABBC-

$\nu$	FP (small $ V_d $ )					LP (large $ V_d $ )					$V_d^{(c)}$ (meV)
	$\nu_{+\uparrow}$	$\nu_{+\downarrow}$	$\nu_{-\uparrow}$	$\nu_{-\downarrow}$	$T$	$\nu_{+\uparrow}$	$\nu_{+\downarrow}$	$\nu_{-\uparrow}$	$\nu_{-\downarrow}$	$T$	
-3	1	0	0	0	$\times$	1	0	0	0	$\times$	\
-2	2	0	0	0	$\times$	1	0	1	0	$\checkmark$	
-1	2	0	1	0	$\times$	1	1	1	0	$\times$	-2, 2
0	2	0	2	0	$\checkmark$	1	1	1	1	$\checkmark$	-3, 3

TABLE III. The symmetry and occupation of groundstate at integer fillings, with or without electric field for ABABBC-stacking CTTBG. Notice that since they all preserve valley U(1),  $T_0$  and  $T_K$  make no difference so we just use  $T$  to denote TRS.

$V_d$ (meV)	0	1	$\geq 2$
-3	$\mathcal{S}_V$	1.99	Same as LP in Table III
	$\mathcal{S}_{s+}$	0.62	
	$\mathcal{S}_{s-}$	0.63	
-2	$\mathcal{S}_V$	3.96	
	$\mathcal{S}_{s+}$	1.25	
	$\mathcal{S}_{s-}$	1.25	
-1	$\mathcal{S}_V$	5.95	
	$\mathcal{S}_{s+}$	1.37	
	$\mathcal{S}_{s-}$	1.37	
0	$\mathcal{S}_V$	7.92	
	$\mathcal{S}_{s+}$	1.49	
	$\mathcal{S}_{s-}$	1.49	

TABLE IV. The symmetry-breaking strength of the groundstates at integer fillings for ABABAB-stacking CTTBG.  $\mathcal{S}_V, \mathcal{S}_{s\pm}$  are the symmetry-breaking strength of valley U(1) and SU(2) $_{\pm}$  defined in Sec. II C.

stacking CTTBG, all four sublattice-valley bands have different Chern numbers ( $\pm 2, \pm 4$ ), thus, IVC order leads to vortices in Moiré BZ, which are disfavored [33, 61].

We then move to the phase diagram at a finite displacement field. The groundstates of CTTBG for two stacking orders under the displacement field are also recorded in Tables III and IV. We find that the displacement field will suppress the IVC order in ABABAB cases. Under a large enough displacement field, the groundstates of both stackings become the layer polarized states (LP). Applying a large enough vertical field separates the two active bands, where the upper/lower bands are mainly contributed by either top or bottom layers, depending on the direction of the electric field. Thus, one can obtain the groundstates with  $V_d = 5$  meV in Tables III and IV by assuming electrons are first layer-polarized and then minimized their interaction energy inside one layer. We do HF calculation at  $V_d$  from 0 to 9 meV and from  $-9$  to 9 meV for each 1 meV for ABABAB stacking order and ABABBC stacking order, respectively, and record the critical electric field  $V_d^{(c)}$  where the groundstates switch between FP and IVC states and LP states in Tables III and IV. We also plot the HF band at each integer filling in Figs. 3 and 4.

### C. Charge density wave states

$\nu$	FP (small $ V_d $ )					LP (large $ V_d $ )					$V_d^{(c)}$ (meV)
	$\nu_{+\uparrow}$	$\nu_{+\downarrow}$	$\nu_{-\uparrow}$	$\nu_{-\downarrow}$	$T$	$\nu_{+\uparrow}$	$\nu_{+\downarrow}$	$\nu_{-\uparrow}$	$\nu_{-\downarrow}$	$T$	
-3.5	0.5	0	0	0	$\times$	0.5	0	0	0	$\times$	\
-2.5	1.5	0	0	0	$\times$	1	0	0.5	0	$\times$	
-1.5	2	0	0.5	0	$\times$	1	0.5	1	0	$\times$	-2, 2
-0.5	2	0.5	0	0	$\times$	1	1	0.5	0	$\times$	-2, 2
	2	0	1.5	0	$\checkmark$	1	1	1	0.5	$\times$	

TABLE V. The symmetry and occupation of groundstate at half-integer fillings, with or without electric field for ABABBC-stacking CTTBG.

$V_d$ (meV)	0	1	$\geq 2$
-3.5	$\mathcal{S}_V$	1.0	Same as LP in Table V
	$\mathcal{S}_{s+}$	0.31	
	$\mathcal{S}_{s-}$	0.31	
-2.5	$\mathcal{S}_V$	2.98	
	$\mathcal{S}_{s+}$	0.94	
	$\mathcal{S}_{s-}$	0.94	
-1.5	$\mathcal{S}_V$	4.95	
	$\mathcal{S}_{s+}$	1.32	
	$\mathcal{S}_{s-}$	1.29	
-0.5	$\mathcal{S}_V$	6.94	
	$\mathcal{S}_{s+}$	1.43	
	$\mathcal{S}_{s-}$	1.43	

TABLE VI. The symmetry-breaking strength of the groundstates at half-integer fillings for ABABAB-stacking CTTBG.  $\mathcal{S}_V, \mathcal{S}_{s\pm}$  are the symmetry-breaking strength of valley U(1) and SU(2) $_{\pm}$  defined in Sec. II C.

In this section, we consider possible translation-symmetry-breaking solutions with fMBZ as shown in Fig. 5(a) and compare their energies to determine the groundstates. Importantly, only after checking that further breaking translation symmetry upon a state will yield the same solution can we verify this state as a groundstate. For example, solutions in  $2 \times 2$  fMBZ are groundstates when the ones in  $4 \times 2$  fMBZ are the same as them, but since we calculate  $4 \times 2$  fMBZ at most if the solutions in  $4 \times 2$  fMBZ have the lowest energy, the true groundstates are not yet determined since other translation-symmetry-breaking states, *e.g.*,  $4 \times 4$  density wave states may be the groundstates.

Using the criterion above, we finally label the fMBZ that groundstate corresponds to with different colors under different displacement fields in Fig. 5(b)(c). We find that the groundstates are translational symmetric states at integer fillings and density wave states at half-integer fillings. For ABABAB stacking CTTBG, the density wave states are all  $2 \times 1$  stripe states while for ABABBC stacking CTTBG, a large enough positive  $V_d$  will prefer further translation-symmetry-breaking than  $2 \times 1$  stripe states. We plot the band structures for  $\nu = -1.5$  as an example in Fig. 6. The translational symmetric solutions at half-integer fillings are always

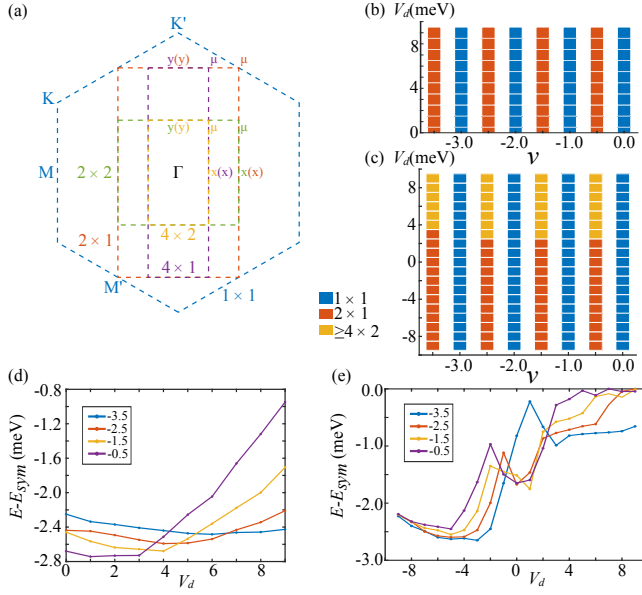


FIG. 5. (a) The folded Brillouin zone considered in this work. (b)(c) The CDW groundstates at all integer and non-integer fillings for ABABAB and ABABBC stacking orders, respectively. (d)(e) Energy difference of  $2 \times 1$  charge density wave states and translational symmetric states at half-integer fillings for ABABAB and ABABBC stacking orders, respectively. Notice that we only plot  $V_d > 0$  cases for ABABAB stacking order due to  $C_{2x}$  symmetry.

gapless as they have partially filled HF bands, as shown in the left panel of Fig. 6(a-e), while breaking translation symmetry tends to open a gap which lowers the total energy. It turns out that if a HF solution is already gapped in  $2 \times 1$  fMBZ, it will be the groundstate, *e.g.*, the  $\nu = -1.5$  states for ABABAB stacking at  $V_d = 0, 5$  meV and ABABBC stacking at  $V_d = 0, -5$  meV as shown in the middle panel of Fig. 6(a)(b)(c)(e). Otherwise, further translation-symmetry-breakings are preferred. Especially, here we find that all these states remain gapless even at  $4 \times 2$  fMBZ, *e.g.*, the  $\nu = -1.5$  states for ABABBC stacking at  $V_d = 5$  meV as shown in Fig. 6(d), which suggests that further translation-symmetry-breaking may happen. We tabulate the groundstates at half-integer fillings for ABABBC and ABABAB stacking in Tables V and VI. We emphasize that Table V is valid only when the groundstates are the solution in  $1 \times 1$  and  $2 \times 1$  fMBZ, since for those cases which have lowest energy in  $4 \times 2$  fMBZ calculation, we do not know whether we have found the groundstate and plot the energy difference of  $2 \times 1$  CDW states and translational symmetric states for two stacking order as a function of electric field in Fig. 5(d)(e). The CDW orders are tuned differently under the electric field for the two stacking orders.

Compared to TBG, where the CDW states are rarely reported except for  $\nu = 3$  [53], CDW states are common as the groundstate in CTTBG, regardless of the stacking order. We attribute this to the distinct charge density profile of the flat band of CTTBG and TBG. As shown in Fig. 2, the distribution of flat band electrons in CTTBG is more spread over the Moiré unit cell, while in TBG, flat band electrons are highly

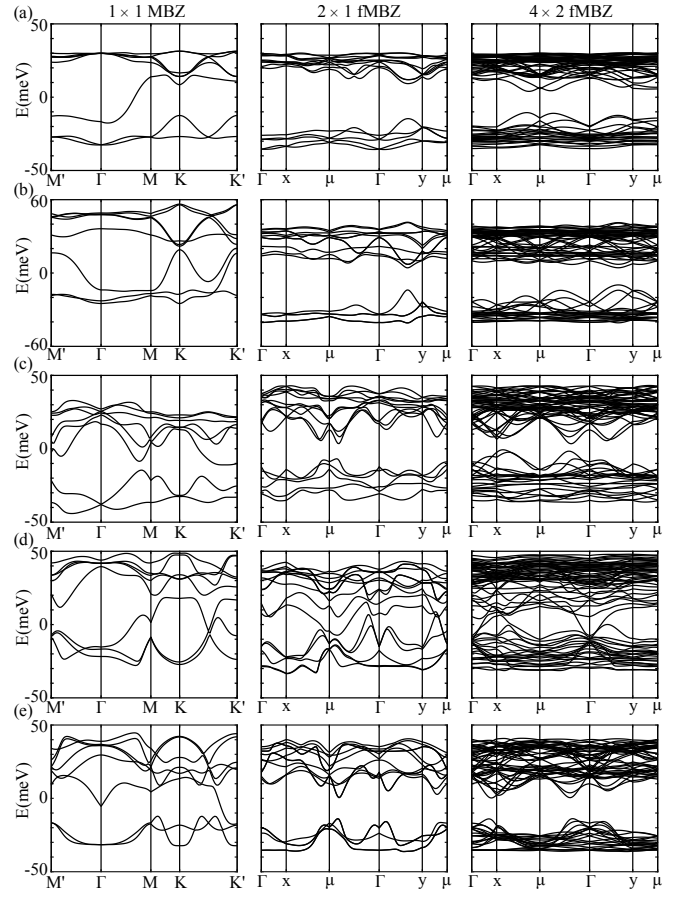


FIG. 6. (a)-(e) The HF bands at  $\nu = -1.5$  for ABABAB stacking CTTBG under  $V_d = 0, 5$  meV and ABABBC stacking CTTBG under  $V_d = 0, 5, -5$  meV, respectively. The bands are calculated in  $1 \times 1, 2 \times 1$  and  $4 \times 2$  fMBZ from left to right in each row. The momentum lattice used is  $8 \times 8$ .

concentrated at the AA-stacking region. The highly localized orbitals in TBG allow one to construct an effective model when nonlocal interactions are negligible, and the correlation effect mostly originates from the on-site Hubbard interaction [36, 38, 39]. In contrast, the nonlocal Coulomb interaction plays a much more crucial role in CTTBG, which avoids electrons occupying neighboring sites and explains the existence of CDW states in CTTBG.

#### IV. SUMMARY AND DISCUSSION

In this work, we study the single-particle physics and mean field phase diagram of CTTBG of two stacking orders, namely ABABAB and ABABBC. We find that there are a pair of flat bands with nontrivial topology at  $\theta = 1.70^\circ$  in these two cases. For ABABBC, we predict the valley Hall effect at fillings  $\pm 4$ . We further perform HF calculation to determine the phase diagram of CTTBG and find that the groundstates are flavor polarized states for ABABBC stacking order and IVC states for ABABAB stacking order at a small displacement



field. Both become layer-polarized states at a large enough displacement field. We find that the groundstates at half-integer fillings are charge density wave states. For ABABAB stacking among a range of displacement fields, the groundstates are always  $2 \times 1$  stripe states. For ABABBC stacking the groundstates are also  $2 \times 1$  stripe states at a small displacement field, and a larger displacement will possibly favor further translation-symmetry-breakings, depending on the direction of the displacement field and filling. We demonstrate that the observed CDW states can originate from the strong Coulomb interaction compared to the small kinetic energy and the real space distribution of the flat band electrons.

We focus on the CDW caused by electron-electron interaction in this work. However, we should point out that this is only a candidate for the mechanism of the CDW states observed in CTTBG [35], and there are other possibilities like

electron-phonon coupling. Further experimental and theoretical research is needed to determine the origin of CDW states in CTTBG.

## ACKNOWLEDGMENTS

Z.-D. S., Y.-J. W. and G.-D. Z. were supported by National Natural Science Foundation of China (General Program No. 12274005), National Key Research and Development Program of China (No. 2021YFA1401900), and Innovation Program for Quantum Science and Technology (No. 2021ZD0302403). X. L. acknowledges support from the National Key R&D Program (Grant nos. 2022YFA1403500/02) and the National Natural Science Foundation of China (Grant Nos. 12274006 and 12141401).

- 
- [1] Yuan Cao, Valla Fatemi, Shiang Fang, Kenji Watanabe, Takashi Taniguchi, Efthimios Kaxiras, and Pablo Jarillo-Herrero, “Unconventional superconductivity in magic-angle graphene superlattices,” *Nature* **556**, 43–50 (2018).
  - [2] Xiaobo Lu, Petr Stepanov, Wei Yang, Ming Xie, Mohammed Ali Aamir, Ipsita Das, Carles Urgell, Kenji Watanabe, Takashi Taniguchi, Guangyu Zhang, Adrian Bachtold, Allan H. MacDonald, and Dmitri K. Efetov, “Superconductors, orbital magnets and correlated states in magic-angle bilayer graphene,” *Nature* **574**, 653–657 (2019).
  - [3] Matthew Yankowitz, Shaowen Chen, Hryhoriy Polshyn, Yuxuan Zhang, K. Watanabe, T. Taniguchi, David Graf, Andrea F. Young, and Cory R. Dean, “Tuning superconductivity in twisted bilayer graphene,” *Science* **363**, 1059–1064 (2019).
  - [4] Aaron L. Sharpe, Eli J. Fox, Arthur W. Barnard, Joe Finney, Kenji Watanabe, Takashi Taniguchi, M. A. Kastner, and David Goldhaber-Gordon, “Emergent ferromagnetism near three-quarters filling in twisted bilayer graphene,” *Science* **365**, 605–608 (2019).
  - [5] Dillon Wong, Kevin P. Nuckolls, Myungchul Oh, Biao Lian, Yonglong Xie, Sangjun Jeon, Kenji Watanabe, Takashi Taniguchi, B. Andrei Bernevig, and Ali Yazdani, “Cascade of electronic transitions in magic-angle twisted bilayer graphene,” *Nature* **582**, 198–202 (2020).
  - [6] Petr Stepanov, Ipsita Das, Xiaobo Lu, Ali Fahimniya, Kenji Watanabe, Takashi Taniguchi, Frank H. L. Koppens, Johannes Lischner, Leonid Levitov, and Dmitri K. Efetov, “Untying the insulating and superconducting orders in magic-angle graphene,” *Nature* **583**, 375–378 (2020).
  - [7] Yu Saito, Jingyuan Ge, Kenji Watanabe, Takashi Taniguchi, and Andrea F. Young, “Independent superconductors and correlated insulators in twisted bilayer graphene,” *Nature Physics* **16**, 926–930 (2020).
  - [8] Myungchul Oh, Kevin P. Nuckolls, Dillon Wong, Ryan L. Lee, Xiaomeng Liu, Kenji Watanabe, Takashi Taniguchi, and Ali Yazdani, “Evidence for unconventional superconductivity in twisted bilayer graphene,” *Nature* **600**, 240–245 (2021).
  - [9] Ipsita Das, Xiaobo Lu, Jonah Herzog-Arbeitman, Zhi-Da Song, Kenji Watanabe, Takashi Taniguchi, B. Andrei Bernevig, and Dmitri K. Efetov, “Symmetry-broken Chern insulators and Rashba-like Landau-level crossings in magic-angle bilayer graphene,” *Nature Physics* **17**, 710–714 (2021).
  - [10] M. Serlin, C. L. Tschirhart, H. Polshyn, Y. Zhang, J. Zhu, K. Watanabe, T. Taniguchi, L. Balents, and A. F. Young, “Intrinsic quantized anomalous Hall effect in a moiré heterostructure,” *Science* **367**, 900–903 (2020).
  - [11] Sameer Grover, Matan Bocarsly, Aviram Uri, Petr Stepanov, Giorgio Di Battista, Indranil Roy, Jiewen Xiao, Alexander Y. Meltzer, Yuri Myasoedov, Keshav Pareek, Kenji Watanabe, Takashi Taniguchi, Binghai Yan, Ady Stern, Erez Berg, Dmitri K. Efetov, and Eli Zeldov, “Chern mosaic and Berry-curvature magnetism in magic-angle graphene,” *Nature Physics* **18**, 885–892 (2022), publisher: Nature Publishing Group.
  - [12] Jiaqi Cai, Eric Anderson, Chong Wang, Xiaowei Zhang, Xiaoyu Liu, William Holtzmann, Yinong Zhang, Fengren Fan, Takashi Taniguchi, Kenji Watanabe, Ying Ran, Ting Cao, Liang Fu, Di Xiao, Wang Yao, and Xiaodong Xu, “Signatures of fractional quantum anomalous Hall states in twisted MoTe<sub>2</sub>,” *Nature* **622**, 63–68 (2023).
  - [13] Heonjoon Park, Jiaqi Cai, Eric Anderson, Yinong Zhang, Jiayi Zhu, Xiaoyu Liu, Chong Wang, William Holtzmann, Chaowei Hu, Zhaoyu Liu, Takashi Taniguchi, Kenji Watanabe, Jiun-Haw Chu, Ting Cao, Liang Fu, Wang Yao, Cui-Zu Chang, David Cobden, Di Xiao, and Xiaodong Xu, “Observation of fractionally quantized anomalous Hall effect,” *Nature* **622**, 74–79 (2023).
  - [14] Fan Xu, Zheng Sun, Tongtong Jia, Chang Liu, Cheng Xu, Chushan Li, Yu Gu, Kenji Watanabe, Takashi Taniguchi, Bingbing Tong, Jinfeng Jia, Zhiwen Shi, Shengwei Jiang, Yang Zhang, Xiaoxue Liu, and Tingxin Li, “Observation of Integer and Fractional Quantum Anomalous Hall Effects in Twisted Bilayer  $\text{MoTe}_2$ ,” *Physical Review X* **13**, 031037 (2023), publisher: American Physical Society.
  - [15] Yihang Zeng, Zhengchao Xia, Kaifei Kang, Jiacheng Zhu, Patrick Knüppel, Chirag Vaswani, Kenji Watanabe, Takashi Taniguchi, Kin Fai Mak, and Jie Shan, “Thermodynamic evidence of fractional Chern insulator in moiré MoTe<sub>2</sub>,” *Nature* **622**, 69–73 (2023), publisher: Nature Publishing Group.
  - [16] Eslam Khalaf, Alex J. Kruchkov, Grigory Tarnopolsky, and Ashvin Vishwanath, “Magic angle hierarchy in twisted graphene multilayers,” *Physical Review B* **100**, 085109 (2019).
  - [17] Miao Liang, Meng-Meng Xiao, Zhen Ma, and Jin-Hua Gao, “Moiré band structures of the double twisted few-layer graphene,” *Physical Review B* **105**, 195422 (2022).

- [18] Jeong Min Park, Yuan Cao, Kenji Watanabe, Takashi Taniguchi, and Pablo Jarillo-Herrero, “Tunable strongly coupled superconductivity in magic-angle twisted trilayer graphene,” *Nature* **590**, 249–255 (2021), publisher: Nature Publishing Group.
- [19] Yuan Cao, Jeong Min Park, Kenji Watanabe, Takashi Taniguchi, and Pablo Jarillo-Herrero, “Pauli-limit violation and re-entrant superconductivity in moiré graphene,” *Nature* **595**, 526–531 (2021), publisher: Nature Publishing Group.
- [20] Zeyu Hao, A. M. Zimmerman, Patrick Ledwith, Eslam Khalaf, Danial Haie Najafabadi, Kenji Watanabe, Takashi Taniguchi, Ashvin Vishwanath, and Philip Kim, “Electric field-tunable superconductivity in alternating-twist magic-angle trilayer graphene,” *Science* **371**, 1133–1138 (2021), publisher: American Association for the Advancement of Science.
- [21] Jeong Min Park, Yuan Cao, Li-Qiao Xia, Shuwen Sun, Kenji Watanabe, Takashi Taniguchi, and Pablo Jarillo-Herrero, “Robust superconductivity in magic-angle multilayer graphene family,” *Nature Materials* **21**, 877–883 (2022), publisher: Nature Publishing Group.
- [22] Hyunjin Kim, Youngjoon Choi, Cyprian Lewandowski, Alex Thomson, Yiran Zhang, Robert Polski, Kenji Watanabe, Takashi Taniguchi, Jason Alicea, and Stevan Nadj-Perge, “Evidence for unconventional superconductivity in twisted trilayer graphene,” *Nature* **606**, 494–500 (2022), publisher: Nature Publishing Group.
- [23] Simon Turkel, Joshua Swann, Ziyang Zhu, Maine Christos, K. Watanabe, T. Taniguchi, Subir Sachdev, Mathias S. Scheurer, Efthimios Kaxiras, Cory R. Dean, and Abhay N. Pasupathy, “Orderly disorder in magic-angle twisted trilayer graphene,” *Science* **376**, 193–199 (2022), publisher: American Association for the Advancement of Science.
- [24] Xiaoxue Liu, Naiyuan James Zhang, K. Watanabe, T. Taniguchi, and J. I. A. Li, “Isospin order in superconducting magic-angle twisted trilayer graphene,” *Nature Physics* **18**, 522–527 (2022), publisher: Nature Publishing Group.
- [25] Cheng Shen, Patrick J. Ledwith, Kenji Watanabe, Takashi Taniguchi, Eslam Khalaf, Ashvin Vishwanath, and Dmitri K. Efetov, “Dirac spectroscopy of strongly correlated phases in twisted trilayer graphene,” *Nature Materials* **22**, 316–321 (2023), publisher: Nature Publishing Group.
- [26] Mikito Koshino, “Band structure and topological properties of twisted double bilayer graphene,” *Physical Review B* **99**, 235406 (2019), publisher: American Physical Society.
- [27] Cheng Shen, Yanbang Chu, QuanSheng Wu, Na Li, Shuopei Wang, Yanchong Zhao, Jian Tang, Jieying Liu, Jinpeng Tian, Kenji Watanabe, Takashi Taniguchi, Rong Yang, Zi Yang Meng, Dongxia Shi, Oleg V. Yazyev, and Guangyu Zhang, “Correlated states in twisted double bilayer graphene,” *Nature Physics* **16**, 520–525 (2020), publisher: Nature Publishing Group.
- [28] Xiaomeng Liu, Zeyu Hao, Eslam Khalaf, Jong Yeon Lee, Yuval Ronen, Hyobin Yoo, Danial Haie Najafabadi, Kenji Watanabe, Takashi Taniguchi, Ashvin Vishwanath, and Philip Kim, “Tunable spin-polarized correlated states in twisted double bilayer graphene,” *Nature* **583**, 221–225 (2020), publisher: Nature Publishing Group.
- [29] Fengcheng Wu and Sankar Das Sarma, “Ferromagnetism and superconductivity in twisted double bilayer graphene,” *Physical Review B* **101**, 155149 (2020), publisher: American Physical Society.
- [30] Minhao He, Yuhao Li, Jiaqi Cai, Yang Liu, K. Watanabe, T. Taniguchi, Xiaodong Xu, and Matthew Yankowitz, “Symmetry breaking in twisted double bilayer graphene,” *Nature Physics* **17**, 26–30 (2021), publisher: Nature Publishing Group.
- [31] Minhao He, Jiaqi Cai, Ya-Hui Zhang, Yang Liu, Yuhao Li, Takashi Taniguchi, Kenji Watanabe, David H. Cobden, Matthew Yankowitz, and Xiaodong Xu, “Symmetry-Broken Chern Insulators in Twisted Double Bilayer Graphene,” *Nano Letters* **23**, 11066–11072 (2023), publisher: American Chemical Society.
- [32] Ruiheng Su, Manabendra Kuiri, Kenji Watanabe, Takashi Taniguchi, and Joshua Folk, “Superconductivity in twisted double bilayer graphene stabilized by WSe<sub>2</sub>,” *Nature Materials* **22**, 1332–1337 (2023), publisher: Nature Publishing Group.
- [33] Trithep Devakul, Patrick J. Ledwith, Li-Qiao Xia, Aviram Uri, Sergio C. de la Barrera, Pablo Jarillo-Herrero, and Liang Fu, “Magic-angle helical trilayer graphene,” *Science Advances* **9**, eadi6063 (2023), publisher: American Association for the Advancement of Science.
- [34] Yves H. Kwan, Patrick J. Ledwith, Chiu Fan Bowen Lo, and Trithep Devakul, “Strong-coupling topological states and phase transitions in helical trilayer graphene,” (2023), arXiv:2308.09706 [cond-mat].
- [35] Wenxuan Wang, Gengdong Zhou, Wenlu Lin, Zuo Feng, Miao Liang, Zaizhe Zhang, Min Wu, Le Liu, Kenji Watanabe, Takashi Taniguchi, Wei Yang, Guangyu Zhang, Kaihui Liu, Jinhua Gao, Yang Liu, Xincheng Xie, Zhida Song Song, and Xiaobo Lu, “Correlated charge density wave insulators in chirally twisted triple bilayer graphene,” to appear (2024).
- [36] Zhi-Da Song and B. Andrei Bernevig, “Magic-Angle Twisted Bilayer Graphene as a Topological Heavy Fermion Problem,” *Physical Review Letters* **129**, 047601 (2022), publisher: American Physical Society.
- [37] Hao Shi and Xi Dai, “Heavy-fermion representation for twisted bilayer graphene systems,” *Physical Review B* **106**, 245129 (2022), publisher: American Physical Society.
- [38] Geng-Dong Zhou, Yi-Jie Wang, Ninghua Tong, and Zhi-Da Song, “Kondo phase in twisted bilayer graphene,” *Physical Review B* **109**, 045419 (2024), publisher: American Physical Society.
- [39] Yi-Jie Wang, Geng-Dong Zhou, Shi-Yu Peng, Biao Lian, and Zhi-Da Song, “Molecular Pairing in Twisted Bilayer Graphene Superconductivity,” (2024), arXiv:2402.00869 [cond-mat].
- [40] Naoto Nakatsuji, Takuto Kawakami, and Mikito Koshino, “Multi-scale lattice relaxation in general twisted trilayer graphenes,” (2023), arXiv:2305.13155 [cond-mat].
- [41] Yves H. Kwan, Jiabin Yu, Jonah Herzog-Arbeitman, Dmitri K. Efetov, Nicolas Regnault, and B. Andrei Bernevig, “Moiré Fractional Chern Insulators III: Hartree-Fock Phase Diagram, Magic Angle Regime for Chern Insulator States, the Role of the Moiré Potential and Goldstone Gaps in Rhombohedral Graphene Superlattices,” (2023), arXiv:2312.11617 [cond-mat].
- [42] Rafi Bistritzer and Allan H. MacDonald, “Moiré bands in twisted double-layer graphene,” *Proceedings of the National Academy of Sciences* **108**, 12233–12237 (2011).
- [43] Jong Yeon Lee, Eslam Khalaf, Shang Liu, Xiaomeng Liu, Zeyu Hao, Philip Kim, and Ashvin Vishwanath, “Theory of correlated insulating behaviour and spin-triplet superconductivity in twisted double bilayer graphene,” *Nature Communications* **10**, 5333 (2019).
- [44] Areg Ghazaryan, Tobias Holder, Erez Berg, and Maksym Serbyn, “Multilayer graphenes as a platform for interaction-driven physics and topological superconductivity,” *Physical Review B* **107**, 104502 (2023), publisher: American Physical Society.
- [45] A. A. Avetisyan, B. Partoens, and F. M. Peeters, “Electric field tuning of the band gap in graphene multilayers,” *Physical Review B* **79**, 035421 (2009).

- [46] Junkai Dong, Taige Wang, Tianle Wang, Tomohiro Soejima, Michael P. Zaletel, Ashvin Vishwanath, and Daniel E. Parker, “Anomalous Hall Crystals in Rhombohedral Multilayer Graphene I: Interaction-Driven Chern Bands and Fractional Quantum Hall States at Zero Magnetic Field,” (2023), arXiv:2311.05568 [cond-mat].
- [47] Nick Bultinck, Eslam Khalaf, Shang Liu, Shubhayu Chatterjee, Ashvin Vishwanath, and Michael P. Zaletel, “Ground State and Hidden Symmetry of Magic-Angle Graphene at Even Integer Filling,” *Physical Review X* **10**, 031034 (2020).
- [48] Yi Zhang, Kun Jiang, Ziqiang Wang, and Fuchun Zhang, “Correlated insulating phases of twisted bilayer graphene at commensurate filling fractions: A Hartree-Fock study,” *Physical Review B* **102**, 035136 (2020).
- [49] Shang Liu, Eslam Khalaf, Jong Yeon Lee, and Ashvin Vishwanath, “Nematic topological semimetal and insulator in magic-angle bilayer graphene at charge neutrality,” *Physical Review Research* **3**, 013033 (2021).
- [50] Y. H. Kwan, G. Wagner, T. Soejima, M. P. Zaletel, S. H. Simon, S. A. Parameswaran, and N. Bultinck, “Kekulé’s Spiral Order at All Nonzero Integer Fillings in Twisted Bilayer Graphene,” *Physical Review X* **11**, 041063 (2021), publisher: American Physical Society.
- [51] Maine Christos, Subir Sachdev, and Mathias S. Scheurer, “Correlated Insulators, Semimetals, and Superconductivity in Twisted Trilayer Graphene,” *Physical Review X* **12**, 021018 (2022).
- [52] Glenn Wagner, Yves H. Kwan, Nick Bultinck, Steven H. Simon, and S. A. Parameswaran, “Global Phase Diagram of the Normal State of Twisted Bilayer Graphene,” *Physical Review Letters* **128**, 156401 (2022), publisher: American Physical Society.
- [53] Fang Xie, Jian Kang, B. Andrei Bernevig, Oskar Vafek, and Nicolas Regnault, “Phase diagram of twisted bilayer graphene at filling factor  $\nu = \pm 3$ ,” *Physical Review B* **107**, 075156 (2023).
- [54] Zhida Song, Zhijun Wang, Wujun Shi, Gang Li, Chen Fang, and B. Andrei Bernevig, “All Magic Angles in Twisted Bilayer Graphene are Topological,” *Physical Review Letters* **123**, 036401 (2019).
- [55] Eric Cancès and Claude Le Bris, “Can we outperform the DIIS approach for electronic structure calculations?” *International Journal of Quantum Chemistry* **79**, 82–90 (2000).
- [56] S. A. Parameswaran, R. Roy, and S. L. Sondhi, “Fractional Chern insulators and the  $\{W\}$ -algebra,” *Physical Review B* **85**, 241308 (2012), publisher: American Physical Society.
- [57] Rahul Roy, “Band geometry of fractional topological insulators,” *Physical Review B* **90**, 165139 (2014), publisher: American Physical Society.
- [58] Zhi-Da Song, Biao Lian, Nicolas Regnault, and B. Andrei Bernevig, “Twisted bilayer graphene. II. Stable symmetry anomaly,” *Physical Review B* **103**, 205412 (2021).
- [59] B. Andrei Bernevig, Zhi-Da Song, Nicolas Regnault, and Biao Lian, “Twisted bilayer graphene. III. Interacting Hamiltonian and exact symmetries,” *Physical Review B* **103**, 205413 (2021).
- [60] Patrick J. Ledwith, Eslam Khalaf, and Ashvin Vishwanath, “Strong coupling theory of magic-angle graphene: A pedagogical introduction,” *Annals of Physics Special issue on Philip W. Anderson*, **435**, 168646 (2021).
- [61] Nick Bultinck, Shubhayu Chatterjee, and Michael P. Zaletel, “Mechanism for Anomalous Hall Ferromagnetism in Twisted Bilayer Graphene,” *Physical Review Letters* **124**, 166601 (2020).
- [62] Jeil Jung and Allan H. MacDonald, “Accurate tight-binding and continuum models for the  $\pi$  bands of bilayer graphene,” *Physical Review B* **89**, 035405 (2014).
- [63] Daniel Parker, Patrick Ledwith, Eslam Khalaf, Tomohiro Soejima, Johannes Hauschild, Yonglong Xie, Andrew Pierce, Michael P. Zaletel, Amir Yacoby, and Ashvin Vishwanath, “Field-tuned and zero-field fractional Chern insulators in magic angle graphene,” (2021), arXiv:2112.13837 [cond-mat].
- [64] Eugene P. Wigner, “Normal Form of Antiunitary Operators,” *Journal of Mathematical Physics* **1**, 409–413 (1960).

## Appendix A: More details about Model and convention

In this section, we derive the continuum model [16, 42] for the chirally twisted triple bilayer graphene (CTTBG) detailedly. As in the main text, the rotation angle of the three bilayers  $i = 1, 2, 3$  are  $(\theta, 0, -\theta)$  from top to bottom. Like the case in twist bilayer graphene (TBG) [42], the low energy states in CTTBG are also contributed by the original low energy states near  $\mathbf{K}, \mathbf{K}'$  point of the untwisted unit, which is the single-layer graphene in TBG and Bernal-stacking bilayer graphene here. We choose the Bloch basis

$$c_{i,\mathbf{p},a} = \frac{1}{\sqrt{N}} \sum_{\mathbf{R}_i} e^{-i\mathbf{p} \cdot \mathbf{R}_{\theta_i}(\mathbf{R}_i + \boldsymbol{\tau}_a + \mathbf{d}_i)} c_{i,\mathbf{R}_i,a} \quad (\text{A1})$$

where  $\mathbf{R}_i$  are lattice vectors of the  $i$ -th bilayers,  $a = l\alpha$  in order (1A,1B,2A,2B) labels the layer index  $l$  in each bilayer graphene and sublattice  $\alpha$  (1 is the top layer and 2 is the bottom layer),  $\boldsymbol{\tau}_a$  is the atom position inside the unit cell while  $\boldsymbol{\tau}_a = \boldsymbol{\tau}_\alpha + \boldsymbol{\tau}_l$  where  $\boldsymbol{\tau}_\alpha, \boldsymbol{\tau}_l$  define the position of sublattice and monolayer graphene inside bilayer. Besides, we define  $\mathbf{d}_i$  to be the displacement for the  $i$ -th bilayer, and if  $\mathbf{d}_i = 0$ , the AB stacking region of the bilayer graphene is located in the origin.  $\mathbf{R}_i, \boldsymbol{\tau}_a, \mathbf{d}_i$  are all measured in the reference frame of each graphene bilayer, which require rotations to be their actual value in the laboratory frame.  $\mathbf{p}$  is defined in the laboratory frame. We choose  $\boldsymbol{\tau}_{1A} - \boldsymbol{\tau}_{1B} = \boldsymbol{\tau}_{2A} - \boldsymbol{\tau}_{2B} = -\frac{a_0}{\sqrt{3}}(0, 1)$  in each layer and for Bernal stacking we have  $\boldsymbol{\tau}_{2B} = \boldsymbol{\tau}_{1A}$  where  $a_0 = 2.46 \text{ \AA}$ .

We adopt the model for each Bernal-stacking bilayer graphene from [43, 62] where the parameters  $\gamma_{0,1,2,3,4}$  and  $\Delta$  are defined in Fig. 7. In the main text we keep only  $\gamma_{0,1}$  and drop the other terms which break the particle hole symmetry  $\mathcal{P}_y$ . The Hamiltonian for the middle layer is

$$H^{(22)}(\mathbf{k}) = \begin{pmatrix} \Delta & -\gamma_0 f(\mathbf{k}) & \gamma_4 f^*(\mathbf{k}) & \gamma_1 \\ -\gamma_0 f^*(\mathbf{k}) & 0 & \gamma_3 f(\mathbf{k}) & \gamma_4 f^*(\mathbf{k}) \\ \gamma_4 f(\mathbf{k}) & \gamma_3 f^*(\mathbf{k}) & 0 & -\gamma_0 f(\mathbf{k}) \\ \gamma_1 & \gamma_4 f(\mathbf{k}) & -\gamma_0 f^*(\mathbf{k}) & \Delta \end{pmatrix} \quad (\text{A2})$$

where  $f(\mathbf{k}) = \sum_{j=1}^3 e^{-i\mathbf{k}\boldsymbol{\delta}_j}$  and  $\boldsymbol{\delta}_j = C_{3z}^{j-1}(\boldsymbol{\tau}_{1A} - \boldsymbol{\tau}_{1B})$ ,  $j = 1, 2, 3$  are the vectors from B site to nearest neighbor A sites. The Hamiltonian for other bilayers could be obtained by

$$H^{(11)}(\mathbf{k}) = H^{(22)}(R_\theta^{-1}\mathbf{k}), H^{(33)}(\mathbf{k}) = H^{(22)}(R_\theta\mathbf{k}). \quad (\text{A3})$$

We have  $f(\eta\mathbf{K} + \mathbf{k}) \approx \frac{\sqrt{3}}{2}a_0(\eta\mathbf{k}_x + i\mathbf{k}_y)$  for small  $|\mathbf{k}|$ . We denote  $h^{(\eta)}(\mathbf{k})$  as the low energy Hamiltonian near  $\eta\mathbf{K}$  such

that  $h^{(\eta)}(\mathbf{k}) = H^{(22)}(\eta\mathbf{K} + \mathbf{k})$ . We then consider hopping between different bilayer graphenes. The hopping term in the two-center, tight-binding approximation is

$$\hat{T}^{ij} = \sum_{\mathbf{R}, \mathbf{R}', \langle aa' \rangle} t [R_{\theta_i}(\mathbf{R} + \boldsymbol{\tau}_a + \mathbf{d}_i) - R_{\theta_j}(\mathbf{R}' + \boldsymbol{\tau}_{a'} + \mathbf{d}_j)] c_{i\mathbf{R}a}^\dagger c_{j\mathbf{R}'a'} \quad (\text{A4})$$

where here  $\langle aa' \rangle$  means  $a$  in the  $i$ -th bilayer and  $a'$  in the  $j$ -th bilayer are in adjacent layers, which should not be confused with nearest neighbor sites, and  $i, j$  are also restricted to adjacent layers. We expand  $t(\mathbf{r}) = \frac{1}{N\Omega} \sum_{\mathbf{q}} e^{i\mathbf{q}\cdot\mathbf{r}} t_{\mathbf{q}}$  where  $\mathbf{q}$  goes over all momentum space, yielding

$$\hat{T}^{ij} = \sum_{\mathbf{p}\mathbf{p}'\mathbf{G}\mathbf{G}'} \sum_{\langle aa' \rangle} \frac{t_{\mathbf{p}+\mathbf{R}_{\theta_i}\mathbf{G}}}{\Omega} \delta_{\mathbf{p}+\mathbf{R}_{\theta_i}\mathbf{G}, \mathbf{p}'+\mathbf{R}_{\theta_j}\mathbf{G}'} e^{i\mathbf{G}\cdot(\boldsymbol{\tau}_a+\mathbf{d}_i)-i\mathbf{G}'\cdot(\boldsymbol{\tau}_{a'}+\mathbf{d}_j)} c_{i\mathbf{p}a}^\dagger c_{j\mathbf{p}'a'} \quad (\text{A5})$$

where  $\mathbf{G}, \mathbf{G}'$  sum over unrotated reciprocal lattice, and  $\mathbf{p}, \mathbf{p}'$  sum over the BZ for the  $i, j$ -th bilayers, denoted as  $\text{BZ}_i$  with reciprocal lattice  $R_{\theta_i}\mathbf{G}$ , respectively.

We first consider only the low energy theory in  $\eta = +$  valley where  $\mathbf{p}, \mathbf{p}'$  are close to  $\mathbf{K} = \frac{4\pi}{3a_0}(1, 0)$  and expand  $\mathbf{p} = R_{\theta_i}\mathbf{K} + \delta\mathbf{p}$  and relabel  $\delta\mathbf{p}$  as  $\mathbf{p}$ . Then the Hamiltonian of the intralayer part is just  $H^{ii}(R_{\theta_i}\mathbf{K} + \mathbf{p}) = h^+(R_{\theta_i}^{-1}\mathbf{p}) \approx h^+(\mathbf{p})$  when  $\theta$  is small[54]. For the interlayer part, since  $t_{\mathbf{q}}$  decays exponentially as  $|\mathbf{q}|$  increases, we keep only  $\mathbf{G} = \mathbf{G}_{1,2,3}$  where  $\mathbf{G}_1 = 0, \mathbf{G}_2 = C_{3z}\mathbf{K} - \mathbf{K}, \mathbf{G}_3 = C_{3z}^2\mathbf{K} - \mathbf{K}$ , which corresponds to the three largest hopping  $\approx t_{\mathbf{K}}, t_{C_{3z}\mathbf{K}}, t_{C_{3z}^2\mathbf{K}}$ . By  $C_{3z}$  they are the same and we denote them as  $w\Omega$ . Taking into the lattice relaxation effect, the hopping is not the same for AA and AB hopping so we use  $w_{aa'}$  instead of a single  $w$ . Furthermore, As  $\mathbf{p}, \mathbf{p}'$  are both close to  $\mathbf{K}^+$  the  $\delta$  function in Eq. (A5) also gives  $\mathbf{G} = \mathbf{G}'$ . So the Moiré hopping term in  $\eta = +$  valley is

$$\hat{T}_+^{ij} = \sum_{\mathbf{p}\mathbf{p}'n} \sum_{\langle aa' \rangle} w_{aa'} e^{i\mathbf{G}_n(\boldsymbol{\tau}_a+\mathbf{d}_i-\boldsymbol{\tau}_{a'}-\mathbf{d}_j)} c_{i\mathbf{p}a}^\dagger c_{j\mathbf{p}'a'} \quad (\text{A6})$$

which can also be explicitly written down as

$$\hat{T}_+^{i,i+1} = \sum_{\mathbf{p}\mathbf{p}'n} \sum_{aa'} \left[ \begin{pmatrix} 0 & 0 \\ 1 & 0 \end{pmatrix} \otimes T_n \right]_{aa'} e^{i\mathbf{G}_n(\boldsymbol{\delta}_1+\mathbf{d}_i-\mathbf{d}_{i+1})} c_{i,\mathbf{p},a}^\dagger c_{i+1,\mathbf{p}-\mathbf{q}_{i,i+1},a'} \quad (\text{A7})$$

$$T_n = w_0\sigma_0 + w_1\sigma_x \cos \frac{2\pi(n-1)}{3} + w_1\sigma_y \sin \frac{2\pi(n-1)}{3} \quad (\text{A8})$$

where  $\mathbf{q}_{ij}^n = R_{\theta_j}\mathbf{G}_n - R_{\theta_i}\mathbf{G}_n$ , satisfying  $\mathbf{q}_{ij}^n = C_{3z}^{(n-1)}\mathbf{q}_{ij}^1$  and  $w_0, w_1$  are interlayer AA and AB couplings. In principle,  $\mathbf{q}_{12}^n = R_{\theta}\mathbf{q}_{23}^n$  instead of  $\mathbf{q}_{23}^n$ , which leads to the moiré of moiré structure. Here, we neglect this effect and let  $\mathbf{q}_{12}^n = \mathbf{q}_{23}^n \equiv \mathbf{q}_n$ , with  $\mathbf{q}_1 = k_\theta(0, -1)$ , where  $k_\theta = 2|\mathbf{K}| \sin \frac{\theta}{2}$ .

Eq. (A6) indicates that an electron with momentum  $\mathbf{p}$  in layer  $i$  can couple to electron in the same bilayer with momentum  $\mathbf{p} + \mathbf{b}_1, \mathbf{p} + \mathbf{b}_2$  via Moiré coupling with other bilayers, where  $\mathbf{b}_1 = \mathbf{q}_2 - \mathbf{q}_1 = k_\theta(\frac{\sqrt{3}}{2}, \frac{3}{2})$ ,  $\mathbf{b}_2 = \mathbf{q}_3 - \mathbf{q}_1 =$

$k_\theta(-\frac{\sqrt{3}}{2}, \frac{3}{2})$ , which form a basis of Moiré reciprocal lattice. We then rewrite  $\mathbf{p}$  in the  $i$ -th layer as  $\mathbf{k} - \mathbf{Q}_i$ , where  $\mathbf{k}$  lies in the first Moiré Brillouin zone (MBZ) and  $\mathbf{Q}_i$  run over the set  $\mathcal{Q}_i$ , which is formed by  $-\mathbf{q}_1, 0, \mathbf{q}_1$  plus Moiré reciprocal lattice for  $i = 1, 2, 3$  respectively. Then the Moiré hopping term becomes

$$\hat{T}_+^{i,i+1} = \sum_{\mathbf{k} \in \text{MBZ}} \sum_{\mathbf{Q} \in \mathcal{Q}_i, \mathbf{Q}' \in \mathcal{Q}_{i+1}} \sum_{aa'} [T_+^{i,i+1}(\mathbf{k})]_{\mathbf{Q},a; \mathbf{Q}',a'} c_{\mathbf{k}\mathbf{Q}a}^\dagger c_{\mathbf{k}\mathbf{Q}'a'} \quad (\text{A9})$$

$$[T_+^{i,i+1}(\mathbf{k})]_{\mathbf{Q},a; \mathbf{Q}',a'} = \sum_n \left[ \begin{pmatrix} 0 & 0 \\ 1 & 0 \end{pmatrix} \otimes T_n \right]_{aa'} e^{i\mathbf{G}_n(\boldsymbol{\delta}_1+\mathbf{d}_i-\mathbf{d}_{i+1})} \delta_{\mathbf{Q}+\mathbf{q}_n, \mathbf{Q}'} \quad (\text{A10})$$

where we have neglected the  $\theta$  dependence in  $H^{ii}$ .

We could see the explicit dependence of the Moiré potential over  $\mathbf{d}$  by performing a gauge transformation  $c_j \rightarrow c_j e^{-i\mathbf{K}\cdot(\mathbf{d}_j-j\boldsymbol{\delta}_1)}$  and writing Eq. (A6) in real space by  $c_{i\mathbf{p}a} = \int d\mathbf{r}^2 e^{-i\mathbf{p}\cdot\mathbf{r}} c_{i\mathbf{r}a}$

$$\hat{T}_+^{i,i+1} = \sum_n \sum_{aa'} \int d^2\mathbf{r} \left[ \begin{pmatrix} 0 & 0 \\ 1 & 0 \end{pmatrix} \otimes T_n \right]_{aa'} e^{iC_{3z}^{n-1}\mathbf{K}\cdot(\boldsymbol{\delta}_1+\mathbf{d}_i-\mathbf{d}_{i+1})+iq_n\cdot\mathbf{r}} c_{i,\mathbf{r},a}^\dagger c_{i+1,\mathbf{r},a'} \quad (\text{A11})$$

$$= \sum_n \sum_{aa'} \int d^2\mathbf{r} \left[ \begin{pmatrix} 0 & 0 \\ 1 & 0 \end{pmatrix} \otimes T_n \right]_{aa'} e^{i\mathbf{q}_n\cdot[\mathbf{r}-\hat{z}\times(\boldsymbol{\delta}_1+\mathbf{d}_i-\mathbf{d}_{i+1})/(2\sin\frac{\theta}{2})]} c_{i,\mathbf{r},a}^\dagger c_{i+1,\mathbf{r},a'} \quad (\text{A12})$$

where we have made use of  $C_{3z}^{n-1}\mathbf{K} \cdot \mathbf{d} = \frac{1}{2\sin\frac{\theta}{2}}(\hat{z} \times \mathbf{q}_n) \cdot \mathbf{d} = \frac{1}{2\sin\frac{\theta}{2}}(\mathbf{d} \times \hat{z}) \cdot \mathbf{q}_n$ . In Eq. (A12) one can see that the Moiré pattern is shifted by  $\hat{z} \times (\mathbf{d}_i - \mathbf{d}_{i+1})/(2\sin\frac{\theta}{2})$  due to the displacement.

We then add the Hamiltonian of valley  $\eta = -$ . By acting TRS on Hamiltonian in  $\eta = +$  valley, we have  $h_{aa'}^-(\mathbf{k} - \mathbf{Q}) = h_{aa'}^{+,*}(-\mathbf{k} + \mathbf{Q})$  and  $[T_-^{i,i+1}(\mathbf{k})]_{\mathbf{Q},a; \mathbf{Q}',a'} = [T_+^{i,i+1}(-\mathbf{k})]_{-\mathbf{Q},a; -\mathbf{Q}',a'}^*$ . The BM Hamiltonian is then

$$\hat{H}_{BM} = \sum_{\mathbf{k} \in \text{MBZ}} \sum_{\mathbf{Q} \in \mathcal{Q}_i} h_{aa'}^\eta(\mathbf{k} - \mathbf{Q}) c_{\mathbf{k}\mathbf{Q}a}^\dagger c_{\mathbf{k}\mathbf{Q}a'} + \sum_\eta \sum_i \hat{T}_\eta^{i,i+1} \quad (\text{A13})$$

Finally, we add the vertical electric field and obtain the total non-interacting Hamiltonian  $\hat{H}_0 = \hat{H}_{BM} + \hat{H}_V$ , where

$$\hat{H}_V = V_d \sum_{\mathbf{k} \in \text{MBZ}} \sum_{\mathbf{Q} \in \mathcal{Q}_i} \left( l_{\mathbf{Q}a} - \frac{7}{2} \right) c_{\mathbf{k}\mathbf{Q}a}^\dagger c_{\mathbf{k}\mathbf{Q}a'} \quad (\text{A14})$$

For  $c_{\mathbf{k}\mathbf{Q}a}^\dagger$ ,  $\mathbf{Q} \in \mathcal{Q}_i$  which comes from  $a$  sublattice and the  $i$ -th bilayer we label the monolayer graphene it belongs to as  $l_{\mathbf{Q}a}$ .

We end this section with a discussion on the influence of the hopping terms  $\gamma_{3,4}$  and  $\Delta$ . We plot the single particle



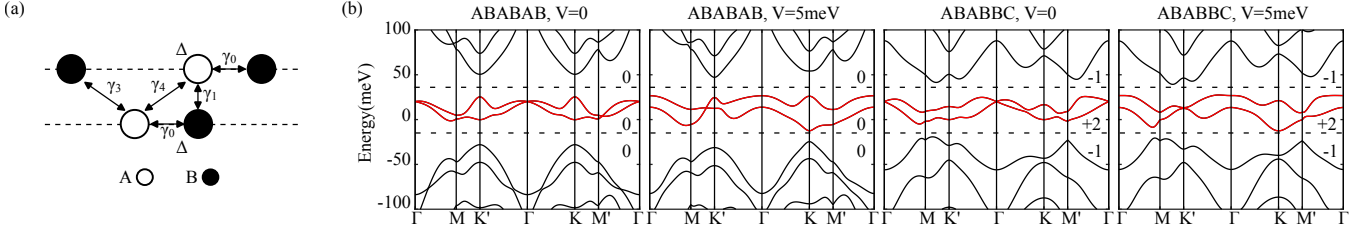


FIG. 7. (a) The definition of tight binding parameters in Bernal bilayer graphene. (b) The single particle band when  $\gamma_3, \gamma_4, \Delta$  are taken into consideration for ABABAB stacking CTTBG under  $V_d = 0, 5 \text{ meV}$  and ABABBC stacking CTTBG under  $V_d = 0, 5 \text{ meV}$  from left to right. The numbers mark the total Chern number of the remote conduction bands, the flat bands and the remote valence bands from top to bottom, respectively.

bands in Fig. 7(b). Compared to Fig. 1(c) where the two flat bands are separated by the displacement, here there is not a gap between them, so the Chern number of each band is not well defined. However, we find that the total Chern number of the flat bands and the remote conduction/valence bands are separately the same as those without  $\gamma_{3,4}, \Delta$ .

## 2. Projected model

The interaction Hamiltonian we consider are

$$\hat{H}_I = \frac{1}{2\Omega_{tot}} \sum_{\mathbf{q} \in \text{MBZ}} \sum_{\mathbf{G}} V(\mathbf{q} + \mathbf{G}) \delta \rho_{\mathbf{q}+\mathbf{G}} \delta \rho_{-\mathbf{q}-\mathbf{G}}, \quad (\text{B1})$$

where  $V(\mathbf{q} + \mathbf{G})$  is the Fourier component of the electron-electron interaction, which we take to be the double-gate-screened Coulomb interaction  $V(\mathbf{q}) = \frac{e^2}{2\epsilon|\mathbf{q}|} \tanh \frac{\xi|\mathbf{q}|}{2}$ , and

$$\delta \rho_{\mathbf{q}+\mathbf{G}} = \sum_{\eta\alpha s} \sum_{\mathbf{k} \in \text{MBZ}} \sum_{\mathbf{Q} \in \mathcal{Q}} \left( c_{\mathbf{k}+\mathbf{q}, \mathbf{Q}-\mathbf{G}, a, \eta, s}^\dagger c_{\mathbf{k}, \mathbf{Q}, a, \eta, s} - \frac{1}{2} \delta_{\mathbf{q}, 0} \delta_{\mathbf{G}, 0} \right) \quad (\text{B2})$$

is the Fourier component of the density operator relative to CNP.

Hereafter we write the total model  $\hat{H}_0 + \hat{H}_I$  on the eigenstate basis of  $\hat{H}_0$

## Appendix B: Projected model and Hatree-Fock calculation

### 1. Gauge fixing

For later convenience, we fix the gauge choice of flat band operators. We expand the electron operators in the eigenstate of  $\hat{H}_0$  into the original basis as  $c_{\mathbf{k}, m, \eta, s}^\dagger = \sum_{\mathbf{Q}, a} u_{\mathbf{Q}, a, m}^{(\eta)}(\mathbf{k}) c_{\mathbf{k}, \mathbf{Q}, a, \eta, s}^\dagger$ , where  $m = \pm 1$  labels the flat bands and  $|m| > 1$  are remote valence/conduction band. We choose the periodical gauge  $c_{\mathbf{k}+\mathbf{G}, m, \eta, s}^\dagger = c_{\mathbf{k}, m, \eta, s}^\dagger$  so  $u_{\mathbf{Q}, a, m}^{(\eta)}(\mathbf{k} + \mathbf{G}) = u_{\mathbf{Q}-\mathbf{G}, a, m}^{(\eta)}(\mathbf{k})$ , and the electrons in two valley are related by  $c_{\mathbf{k}, m, \eta, s}^\dagger = T_0 c_{-\mathbf{k}, m, -\eta, s}^\dagger T_0^{-1}$  so  $u_{\mathbf{Q}, a, m}^{(\eta)}(\mathbf{k}) = u_{-\mathbf{Q}, a, m}^{(-\eta)*}(-\mathbf{k})$ .

$$\hat{H}_0 = \sum_{\mathbf{k} \in \text{MBZ}} \sum_{\eta, m, s} \epsilon_m^{(\eta)}(\mathbf{k}) c_{\mathbf{k}, m, \eta, s}^\dagger c_{\mathbf{k}, m, \eta, s} \quad (\text{B3})$$

and  $\hat{H}_I$  keeps the form in Eq. (B1) with density operator becoming

$$\delta \rho_{\mathbf{q}+\mathbf{G}} = \sum_{\mathbf{k}, \eta, s} \sum_{mn} M_{mn}^{(\eta)}(\mathbf{k}; \mathbf{q} + \mathbf{G}) \left( c_{\mathbf{k}+\mathbf{q}, m, \eta, s}^\dagger c_{\mathbf{k}, n, \eta, s} - \frac{1}{2} \delta_{\mathbf{q}, 0} \delta_{mn} \right) \quad (\text{B4})$$

$$M_{mn}^{(\eta)}(\mathbf{k}; \mathbf{q} + \mathbf{G}) = \sum_{\mathbf{Q}, a} u_{\mathbf{Q}-\mathbf{G}, a, m}^{(\eta)*}(\mathbf{k} + \mathbf{q}) u_{\mathbf{Q}, a, n}^{(\eta)}(\mathbf{k}) \quad (\text{B5})$$

Substitute Eq. (B4) into Eq. (B1) we have

$$\hat{H}_I = \frac{1}{2\Omega_{tot}} \sum_{\mathbf{k}, \mathbf{k}' \in \text{MBZ}} \sum_{ss'} \sum_{\eta\eta'} U_{mn, m'n'}^{(\eta\eta')}(\mathbf{q}; \mathbf{k}, \mathbf{k}') \left( c_{\mathbf{k}+\mathbf{q}, m, \eta, s}^\dagger c_{\mathbf{k}, n, \eta, s} - \frac{1}{2} \delta_{\mathbf{q}, 0} \delta_{mn} \right) \left( c_{\mathbf{k}'-\mathbf{q}, m', \eta', s'}^\dagger c_{\mathbf{k}', n', \eta', s'} - \frac{1}{2} \delta_{\mathbf{q}, 0} \delta_{m'n'} \right) \quad (\text{B6})$$

$$U_{mn, m'n'}^{(\eta\eta')}(\mathbf{q}; \mathbf{k}, \mathbf{k}') = \sum_{\mathbf{G}} V(\mathbf{q} + \mathbf{G}) M_{mn}^{(\eta)}(\mathbf{k}, \mathbf{q} + \mathbf{G}) M_{m'n'}^{(\eta')}(\mathbf{k}', -\mathbf{q} - \mathbf{G}) \quad (\text{B7})$$

To write down the effect model on the flat bands, we only keep  $m, n$  for the flat bands in Eqs. (B3) and (B6). One should notice that this is not directly projecting Eq. (B6) on the flat band, where HF potential from the remote bands should also be included. In fact, the actual interaction term we consider includes not only Eq. (B1) but also a subtraction term in order to avoid double counting of the interactions included in DFT bands and HF calculation, as done in previous works in Moiré materials. Readers can refer to the appendices of Ref.[41, 63] which discuss this in detail. In short, the subtraction lets the HF contribution of  $\hat{H}_I$  to the energy bands vanish at a certain reference density. One can check that our procedure here is just the infinite temperature subtraction scheme in Ref.[63], where the Hatree-Fock decomposition vanishes when the active bands are all half-filled, the remote valence bands are fully filled and remote conductance bands are empty.

We also summarized the symmetry, hermicity, and periodicity of  $M$  and  $U$  here, which can be used to check the correctness of numerical results.

- By time reversal symmetry we have  $M_{mn}^{(-\eta)}(\mathbf{k}; \mathbf{q} + \mathbf{G}) = M_{mn}^{(\eta)*}(-\mathbf{k}; -\mathbf{q} - \mathbf{G})$ .
- With the periodicity in reciprocal space we have  $M_{mn}^{(\eta)}(\mathbf{k} + \mathbf{G}'; \mathbf{q} + \mathbf{G}) = \sum_{\mathbf{Q}_a} u_{\mathbf{Q}-\mathbf{G}-\mathbf{G}'a,m}^{(\eta)*}(\mathbf{k} + \mathbf{q}) u_{\mathbf{Q}-\mathbf{G}'a,n}^{(\eta)}(\mathbf{k}) = M_{mn}^{(\eta)}(\mathbf{k}; \mathbf{q} + \mathbf{G})$ .  $U_{mn,m'n'}^{(\eta')}(\mathbf{q}; \mathbf{k}, \mathbf{k}')$  is periodical in reciprocal space for

both  $\mathbf{q}, \mathbf{k}, \mathbf{k}'$ .

- By hermicity we have  $M_{mn}^{(\eta)*}(\mathbf{k}; \mathbf{q} + \mathbf{G}) = M_{nm}^{(\eta)}(\mathbf{k} + \mathbf{q} + \mathbf{G}; -\mathbf{q} - \mathbf{G}) = M_{nm}^{(\eta)}(\mathbf{k} + \mathbf{q}; -\mathbf{q} - \mathbf{G})$ ,  $U_{mn,men's}^{(\eta\eta')*}(\mathbf{q}; \mathbf{k}, \mathbf{k}') = U_{n'm',nm}^{(\eta'\eta)}(\mathbf{q}; \mathbf{k}' - \mathbf{q}, \mathbf{k} + \mathbf{q})$
- Since  $V(\mathbf{q}) = V(-\mathbf{q})$ , we have  $U_{mn,m'n'}^{(\eta\eta')}(\mathbf{q}; \mathbf{k}, \mathbf{k}') = U_{m'n',mn}^{(\eta'\eta)}(-\mathbf{q}; \mathbf{k}', \mathbf{k})$  as we have summed over infinite  $\mathbf{G}$ .

Notice that some properties above depend on summing over infinite  $\mathbf{Q}$  in Eq. (B5) and infinite  $\mathbf{G}$  in Eq. (B7), so in the numerical calculation where only finite  $\mathbf{Q}, \mathbf{G}$  are used they are not exactly satisfied but the deviation will decay as the cutoff increases.

### 3. Hatree-Fock method

We perform the Hatree-Fock calculation in momentum space on  $\hat{H}_0 + \hat{H}_I$ . Spontaneous breaking of the translation symmetry is allowed, and the order parameters are  $O_{bm\eta s, b'n\eta' s'}(\mathbf{k}) = \langle c_{\mathbf{k}+\mathbf{Q}_b, m, \eta, s}^\dagger c_{\mathbf{k}+\mathbf{Q}_{b'}, n, \eta', s'} \rangle - \frac{1}{2} \delta_{bb'} \delta_{mn} \delta_{ss'} \delta_{\eta\eta'}$ . The mean field Hamiltonian depends only on  $O_{bm\eta s, b'n\eta' s'}(\mathbf{k})$ :

$$\hat{H}_I^{MF} = \frac{1}{\Omega_{tot}} \sum_{\mathbf{k} \in \text{fMBZ}} \sum_{bb'} \sum_{m\eta s, n\eta' s'} (H_I^{MF})_{bm\eta s, b'n\eta' s'}(\mathbf{k}) c_{\mathbf{k}+\mathbf{Q}_b, m\eta s}^\dagger c_{\mathbf{k}+\mathbf{Q}_{b'}, n\eta' s'} \quad (\text{B8})$$

where

$$(H_I^{MF})_{bm\eta s, b'n\eta' s'}(\mathbf{k}) = \sum_{b''b'''} \sum_{m'n'} \sum_{\mathbf{k}'} \left[ \delta_{ss'} \delta_{\eta\eta'} \sum_{\eta''s''} U_{mnbb'; m'n'b''b'''}^{(H, \eta\eta'')}(\mathbf{k}, \mathbf{k}') O_{b''m'\eta''s'', b''m'n'\eta''s''}(\mathbf{k}') \right. \\ \left. + U_{mnbb'; m'n'b''b'''}^{(F, \eta\eta')}(\mathbf{k}, \mathbf{k}') O_{b''m'\eta's', b''m'n'\eta's'}(\mathbf{k}') \right] \quad (\text{B9})$$

$$U_{mnbb'; m'n'b''b'''}^{(H, \eta\eta'')}(\mathbf{k}, \mathbf{k}') = \sum_{\mathbf{G}} U_{mn, m'n'}^{(\eta\eta'')}(\mathbf{Q}_b - \mathbf{Q}_{b'}; \mathbf{k} + \mathbf{Q}_{b'}, \mathbf{k}' + \mathbf{Q}_{b'''}) \delta_{\mathbf{Q}_b - \mathbf{Q}_{b'} + \mathbf{Q}_{b''} - \mathbf{Q}_{b'''}, \mathbf{G}} \quad (\text{B10})$$

$$U_{mnbb'; m'n'b''b'''}^{(F, \eta\eta')}(\mathbf{k}, \mathbf{k}') = - \sum_{\mathbf{G}} U_{mn, m'n'}^{(\eta\eta')}(\mathbf{k} - \mathbf{k}' - \mathbf{Q}_{b'''} + \mathbf{Q}_b; \mathbf{k}' + \mathbf{Q}_{b'''}, \mathbf{k} + \mathbf{Q}_{b'}) \delta_{\mathbf{Q}_b - \mathbf{Q}_{b'} + \mathbf{Q}_{b''} - \mathbf{Q}_{b'''}, \mathbf{G}} \quad (\text{B11})$$

The interaction energy can be written as

$$\langle \hat{H}_I \rangle = \frac{1}{2} \frac{1}{\Omega_{tot}} \sum_{\mathbf{k} \in \text{fMBZ}} \sum_{bb'} \sum_{m\eta s, n\eta' s'} (H_I^{MF})_{bm\eta s, b'n\eta' s'}(\mathbf{k}) O_{bm\eta s, b'n\eta' s'}(\mathbf{k}) + \text{const}' \quad (\text{B12})$$

where we have also neglected a constant term that does not depend on order parameters. Together with  $\hat{H}_0$  (Eq. (B3)) in the fMBZ

$$(H_0)_{bm\eta s, b'm'\eta' s'} = \epsilon_n^{(\eta)}(\mathbf{k} + \mathbf{Q}_b) \delta_{bb'} \delta_{mm'} \delta_{\eta\eta'} \delta_{ss'}. \quad (\text{B13})$$

The matrix element for total mean field Hamiltonian is  $(H_0)_{bm\eta s, b'm'\eta' s'} + \Delta_{bm\eta s, b'm'\eta' s'}$  and the total energy is

$$E_{tot} = \text{Tr} \left[ \left( H_0 + \frac{1}{2} H_I^{MF} \right) O^T \right] \quad (\text{B14})$$

where the trace is taken over spin, band, momentum in fMBZ, and the translation-symmetry-breaking momentum.

#### 4. Classifying the order parameters

In this section we prove that  $\mathcal{S}_V, \mathcal{S}_{s\pm}$  are invariant under  $U(2) \times U(2)$  symmetry. The invariance under charge  $U(1)$  is trivial. To see the other symmetry properties, we notice that  $\|A\|^2 \equiv \text{Tr}(A^\dagger A)$  is invariant when  $A$  undergoes unitary transformation  $A \rightarrow UAU^\dagger$ . We will drop the index of  $\mathbf{k}$ ,  $b$  temporarily as these symmetry operations does not change momentum. Thus if  $[\Theta, \Theta'] = 0$  under rotation  $\| [O, \Theta] \|^2 \rightarrow \| [e^{i\theta\Theta'} O e^{-i\theta\Theta'}, \Theta] \|^2 = \| e^{i\theta\Theta'} [O, \Theta] e^{-i\theta\Theta'} \|^2 = \| [O, \Theta] \|^2$  is also invariant. From this one can easily see  $\mathcal{S}_V$  is not affected by  $U(1)_V, \text{SU}(2)_\pm$ , and  $\mathcal{S}_{s\pm}$  are not affected by  $U(1)_V$ .

We then consider the transformation of  $\mathcal{S}_{s\pm}$  under spin-SU(2). We first prove the useful identity

$$\sum_i \| [O, \sigma\tau\varsigma_i] \|^2 = \sum_i \| [O, \sigma\tau e^{-i\theta \cdot \varsigma_i} e^{i\theta \cdot \varsigma_i}] \|^2 \quad (\text{B15})$$

for any two by two Hermitian matrix  $\sigma, \tau$  and  $\theta = (\theta_1, \theta_2, \theta_3), \varsigma = (\varsigma_x, \varsigma_y, \varsigma_z)$ . Eq. (B15) hold for any finite  $\theta$  if it is valid for infinitesimal  $\theta$ , which can be verified by keeping only the first order term of  $\theta$  as

$$\begin{aligned} & \sum_i \| [O, \sigma\tau e^{-i\theta \cdot \varsigma_i} e^{i\theta \cdot \varsigma_i}] \|^2 - \sum_i \| [O, \sigma\tau\varsigma_i] \|^2 \\ &= \sum_i \| [O, \sigma\tau (s_i - i[\theta \cdot \varsigma, \varsigma_i])] \|^2 - \sum_i \| [O, \sigma\tau\varsigma_i] \|^2 \\ &= \sum_i 2\text{Tr}([O, \sigma\tau\varsigma_i][O, \sigma\tau[\theta \cdot \varsigma, \varsigma_i]]) \\ &= \sum_{ijk} 2\theta_j \epsilon_{jik} \text{Tr}([O, \sigma\tau\varsigma_i][O, \sigma\tau\varsigma_k]) \\ &= 0 \quad (i \leftrightarrow k \text{ and } \text{Tr}AB = \text{Tr}BA). \end{aligned} \quad (\text{B16})$$

We then calculate  $\mathcal{S}_{s\pm}$  under spin-SU(2) $_\pm$ :

$$\begin{aligned} \mathcal{S}' &= \frac{1}{4} \sum_i \| [e^{i\sigma_0\tau_{v'}\theta \cdot \varsigma} O e^{-i\sigma_0\tau_{v'}\theta \cdot \varsigma}, \sigma_0\tau_{v'}\varsigma_i] \|^2 \\ &= \frac{1}{4} \sum_i \| e^{i\sigma_0\tau_{v'}\theta \cdot \varsigma} [O, e^{-i\sigma_0\tau_{v'}\theta \cdot \varsigma} \sigma_0\tau_{v'}\varsigma_i e^{i\sigma_0\tau_{v'}\theta \cdot \varsigma}] \|^2 \\ &= \frac{1}{4} \sum_i \| [O, \sigma_0 e^{-i\sigma_0\tau_{v'}\theta \cdot \varsigma} \tau_{v'}\varsigma_i e^{i\sigma_0\tau_{v'}\theta \cdot \varsigma}] \|^2 \end{aligned} \quad (\text{B17})$$

where  $v, v' = \pm$ . Since  $\tau_{v'}^2 = \tau_v$  for  $v' = \pm$ , one has  $e^{i\tau_{v'}\theta \cdot \varsigma} = \sum_{n=0}^{\infty} \frac{(i\tau_{v'}\theta \cdot \varsigma)^n}{n!} = \tau_0\varsigma_0 + \tau_{v'} \sum_{n=1}^{\infty} \frac{(i\theta \cdot \varsigma)^n}{n!} = \tau_0\varsigma_0 - \tau_{v'}\varsigma_0 + \tau_{v'} e^{i\theta \cdot \varsigma}$ . Then we have

$$e^{-i\tau_{v'}\theta \cdot \varsigma} \tau_{v'}\varsigma_i e^{i\tau_{v'}\theta \cdot \varsigma} = \tau_v [(\tau_0 - \tau_{v'})\varsigma_i + \tau_{v'} e^{-i\theta \cdot \varsigma} \varsigma_i e^{i\theta \cdot \varsigma}] \quad (\text{B18})$$

The physical meaning is simple:  $\tau_{v'}$  is a projection matrix, and we only perform spin-SU(2) rotation on the subspace that  $\tau_{v'}$  projecting to, and the action on the complement is identity. Then making use of Eqs. (B15), (B17) and (B18) we have

- for  $v = v' = \pm$ , which corresponds to  $\mathcal{S}_{s\pm}$  transformed under spin SU(2) rotation in  $\pm$  valley,  $\mathcal{S}'_{s\pm} = \sum_i \| [O, \sigma_0\tau_{\pm} e^{-i\theta \cdot \varsigma_i} e^{i\theta \cdot \varsigma_i}] \|^2 = \sum_i \| [O, \sigma_0\tau_{\pm}\varsigma_i] \|^2 = \mathcal{S}_{s\pm}$
- for  $v = -v' = \pm$ , which corresponds to  $\mathcal{S}_{s\pm}$  transformed under spin SU(2) rotation in  $\mp$  valley  $\mathcal{S}'_{s\pm} = \sum_i \| [O, \sigma_0\tau_{\pm}\varsigma_i] \|^2 = \mathcal{S}_{s\pm}$

Performing a gauge transformation among the two flat bands in valley  $v$  means a unitary transformation of the order parameter  $O \rightarrow e^{-i\theta \cdot \sigma\tau_v} O e^{i\theta \cdot \sigma\tau_v}$  when  $v = \pm$ . We can prove that  $\mathcal{S}_{V,s\pm}$  are also invariant under this gauge transformation. The matrix  $\Theta$  for generators included in  $\mathcal{S}_{V,s\pm}$  takes the form  $\sigma_0\tau_v\varsigma_\mu$  for  $v = 0, \pm$  and  $\mu = 0, x, y, z$ . We have

$$\begin{aligned} & \| [e^{-i\theta \cdot \sigma\tau_v} O e^{i\theta \cdot \sigma\tau_v}, \sigma_0\tau_{v'}\varsigma_\mu] \|^2 \\ &= \| [O, \sigma_0 e^{i\theta \cdot \sigma\tau_v} \tau_{v'} e^{-i\theta \cdot \sigma\tau_v} \varsigma_\mu] \|^2 \\ &= \| [O, \sigma_0\tau_{v'}\varsigma_\mu] \|^2 \end{aligned} \quad (\text{B19})$$

we have used  $[\tau_v, \tau_{v'}] = 0$  in the second line.

#### 5. Degeneracy from the HF energy functional

There are some different states that are not related by symmetries but are degenerate at the HF level, which has been mentioned in earlier results in TBG [34, 48]. For example, the authors of Ref.[48] had found that at  $\nu = 0$  there are valley-polarized states, spin-polarized states and spin-valley-locked states which are degenerate and they are named the generalized ferromagnetic insulating states (FMI). Here, we prove that for state with order parameters  $O_{bm\eta s, b'm'\eta' s}(\mathbf{k})$  diagonalized in spin degree of freedom, applying spinless  $T_0$  on one spin sector does not change the total energy. It is worth noticing that this operation is not a symmetry as the Wigner theorem [64] states that any symmetry should be either a unitary operator or an anti-unitary operator, which is not satisfied by this operation. Furthermore, by  $\text{SU}(2)_+ \times \text{SU}(2)_-$  symmetry for all the spin-polarized states that are not polarized in  $z$  direction, we can also rotate the spin polarization to  $z$  direction and apply the same operation. Thus, two sets of states are related.

Under this operation we obtain a new order paraters  $O'$  where  $O'_{bm\eta\uparrow, b'm'\eta'\uparrow}(\mathbf{k}) = O_{bm\eta\uparrow, b'm'\eta'\uparrow}(\mathbf{k})$  and  $O'_{bm\eta\downarrow, b'm'\eta'\downarrow}(\mathbf{k}) = O_{bm\eta\downarrow, b'm'\eta'\downarrow}^*(-\mathbf{k})$ . We have use the notation  $\bar{b}$  such that  $\mathbf{Q}_{\bar{b}} = -\mathbf{Q}_b$  module reciprocal lattice. We write the order parameters as  $O = O_{\uparrow\uparrow}\delta_{s,\uparrow} + O_{\downarrow\downarrow}\delta_{s,\downarrow}$ . We demonstrate the three terms in total energy are unchanged one by one:

- the kinetic term.  $\hat{H}_0$  is diagonalized in spin subspace, and the total kinetic energy is the summation of the kinetic energy of spin up and spin down subspace, and each of them is unchanged under  $T_0$ .
- the Hartree term. For the Hartree term, this proof consists of two steps: 1.  $O$  and  $O'$  give the same Hartree potential, which preserves  $T_0$  and is diagonal in the spin subspace. 2. For Hamiltonian preserving  $T_0$  and diagonal in spin subspace, we repeat the argument for the kinetic term.
- the Fock term. From Eq. (B11) one can see that when

the order parameters are diagonalized in spin subspace, the Fock term of mean field Hamiltonian are also diagonalized in spin subspace, by which we write it as  $\Delta_{\uparrow\uparrow}^F$  and  $\Delta_{\downarrow\downarrow}^F$  and  $\Delta_{ss}^F$  depends only on  $O_{ss}$ . As  $T_0$  is the symmetry of the Hamiltonian, acting  $T_0$  does not change the Fock energy  $\frac{1}{2} \sum_s \text{Tr}[\Delta_{ss}^F O_{ss}]$ . Meanwhile  $T_0$  does not flip spin, so each term  $\frac{1}{2} \text{Tr}[\Delta_{ss}^F O_{ss}]$  is separately invariant when we apply  $T_0$  to each spin sector.